Ultracold fermions in a graphene-type optical lattice

Kean Loon Lee (李健伦),[1,2,3,][*] Benoît Grémaud,[2,1,4] Rui Han (韩睿),[1] Berthold-Georg Englert,[1,4] and Christian Miniatura[5,1,4]

[1]*Centre for Quantum Technologies, National University of Singapore, 3 Science Drive 2, Singapore 117543, Singapore*
[2]*Laboratoire Kastler-Brossel, UPMC-Paris 6, ENS, CNRS; 4 Place Jussieu, F–75005 Paris, France*
[3]*NUS Graduate School for Integrative Sciences and Engineering, National University of Singapore, Singapore 117597, Singapore*
[4]*Department of Physics, National University of Singapore, 2 Science Drive 3, Singapore 117542, Singapore*
[5]*Institut Non Linéaire de Nice, UMR 6618, UNS, CNRS; 1361 route des Lucioles, 06560 Valbonne, France*
(Received 23 June 2009; published 19 October 2009)

Some important features of the graphene physics can be reproduced by loading ultracold fermionic atoms in a two-dimensional optical lattice with honeycomb symmetry and we address here its experimental feasibility. We analyze in great detail the optical lattice generated by the coherent superposition of three coplanar running laser waves with respective angles $2\pi/3$. The corresponding band structure displays Dirac cones located at the corners of the Brillouin zone and close to half-filling this system is well described by massless Dirac fermions. We characterize their properties by accurately deriving the nearest-neighbor hopping parameter t_0 as a function of the optical lattice parameters. Our semiclassical instanton method proves in excellent agreement with an exact numerical diagonalization of the full Hamilton operator in the tight-binding regime. We conclude that the temperature range needed to access the Dirac fermions regime is within experimental reach. We also analyze imperfections in the laser configuration as they lead to optical lattice distortions which affect the Dirac fermions. We show that the Dirac cones do survive up to some critical intensity or angle mismatches which are easily controlled in actual experiments. In the tight-binding regime, we predict, and numerically confirm, that these critical mismatches are inversely proportional to the square root of the optical potential strength. We also briefly discuss the interesting possibility of fine tuning the mass of the Dirac fermions by controlling the laser phase in an optical lattice generated by the incoherent superposition of three coplanar independent standing waves with respective angles $2\pi/3$.

I. INTRODUCTION

In 2004, researchers in Manchester isolated one-atom thick sheets of carbon atoms, with the atoms organized in a planar honeycomb structure [1]. Such a material is referred to as graphene and is of utmost importance in condensed-matter physics since by stacking it one gets the graphite structure and by wrapping it one gets carbon nanotubes and fullerenes [2]. Graphene is also of great theoretical interest because it provides a physical realization of two-dimensional field theories with quantum anomalies [3]. Indeed, the effective theory that describes the low-energy electronic excitations in graphene is that of two-dimensional massless Weyl-Dirac fermions. In graphene these massless fermions propagate with about one 300th of the speed of light. Triggered by the Manchester discovery, an intense activity has flourished in the field, and continues to flourish, as witnessed by Refs. [4–9], for example. The reported and predicted phenomena include the Klein paradox (the perfect transmission of relativistic particles through high and wide potential barriers) [7], the anomalous quantum Hall effect induced by Berry phases [10,11], and its corresponding modified Landau levels [12].

It is now well established that some condensed-matter phenomena can be reproduced by loading ultracold atoms into optical lattices [13,14]. The great advantage is that the relevant parameters (shape and strength of the light potential,

atom-atom interaction strength via Feshbach resonances [15], etc.) are accessible and can be accurately controlled while spurious effects that destroy the quantum coherence are absent such as the analog of the electron-phonon interaction. In [16], Zhu *et al.* proposed to observe Dirac fermions with cold atoms in a hexagonal optical lattice. Our present objective is to analyze in detail this scheme capable of reproducing in atomic physics the unique situation found in graphene. It consists of creating a two-dimensional honeycomb optical lattice and loading it with ultracold fermions such as the neutral ^{6}Li or ^{40}K atoms.

Parts of this paper recall known results. In addition to the need of setting the stage and introducing the notational conventions, there is also the intention to bridge the solid-state community and the atomic physics community on the particular subject of massless Dirac fermions as observed in graphene sheets and its counterpart in atomic physics. We also present extensions of previous solid-state works in the atomic physics context and report a number of results.

We analyze the various experimental parameters that need to be controlled in order to reproduce, with cold atoms trapped in an optical lattice, the physics at work in graphene. After briefly introducing optical lattices, we first explain how to create an optical lattice with the honeycomb symmetry and analyze its crystallographic features. We then calculate the band structure in the tight-binding approximation and by exact diagonalization, thereby providing evidence for the occurrence of the so-called Dirac points. Next, we evaluate the nearest-neighbor hopping amplitude by using a semiclassical instanton method. For the benefit of possible experiments we

_____
[*]leekeanl@sps.nus.edu.sg

give the necessary requirements for reaching the massless
Dirac fermion regime. Finally, we examine how massless
Dirac fermions survive lattice distortions that could result
from intensity-unbalanced or misaligned laser beams. These
distortions open the way to new physics related to the quantum Hall effect [17]. We will close by briefly mentioning
possible experiments to target for noninteracting and interacting ultracold fermions [18,19].

II. HONEYCOMB OPTICAL LATTICE

A. Radiative forces and optical lattices

A two-level atom (with angular frequency separation ω_{at}
and excited-state angular frequency width Γ) that interacts
with a monochromatic laser field with complex amplitude
$\mathcal{E}(\boldsymbol{r},t)=\boldsymbol{E}(\boldsymbol{r})e^{-i\omega_L t}$ gets polarized and experiences radiative
forces due to photon absorption and emission cycles [20,21].
When the light frequency is tuned far away from the atomic
resonance, i.e., when the light detuning $\delta=\omega_L-\omega_{at}$ is much
larger than Γ, the field-induced saturation effects are negligible and the atom essentially keeps staying in its ground
state. In this situation, the atom-field interaction is dominated
by stimulated emission processes where the atomic dipole
absorbs a photon from one Fourier component of the field
and radiates it back into the same or another one of these
Fourier modes. In each such stimulated cycle, there is a momentum transfer to the atom and, as a net result, the atom
experiences an average force in the course of time. This dipole force exerted by the field onto the atom in its ground
state is conservative. It derives from the polarization energy
shift of the atomic levels (ac Stark or light shifts) [22] and
the dipole potential $V(\boldsymbol{r})$ is given by

$$V(\boldsymbol{r}) = \frac{\hbar\Gamma}{8}\frac{\Gamma}{\delta}\frac{I(\boldsymbol{r})}{I_s}, \qquad (1)$$

where $I(\boldsymbol{r})=\epsilon_0 c|\boldsymbol{E}(\boldsymbol{r})|^2/2$ is the light field intensity (time-
averaged energy current density) at the center-of-mass position $\boldsymbol{r}$ of the atom and I_s is the saturation intensity of the
atom under consideration.

For multilevel atoms, the situation is more complicated as
the dipole potential now depends on the particular atomic
ground state sublevel under consideration. However, if the
laser detuning δ is much larger than the fine and hyperfine
structure splittings of the atomic electronic transition, then
all ground-state atomic sublevels will essentially experience
the same dipole potential. This common potential turns out to
be given by Eq. (1) as well. Hence, by conveniently tailoring
the space and time dependence of the laser field, one can
produce a great variety of dipole potentials and thus manipulate the ground-state atomic motion.

Optical lattices are periodic intensity patterns of light obtained through the interference of several monochromatic laser beams [23]. By loading ultracold atoms into such artificial crystals of light one obtains periodic arrays of atoms.
Indeed, as seen from Eq. (1), when the light field is blue-
detuned from the atomic resonance ($\delta>0$), then the atoms
can be trapped in the field-intensity minima whereas for red-
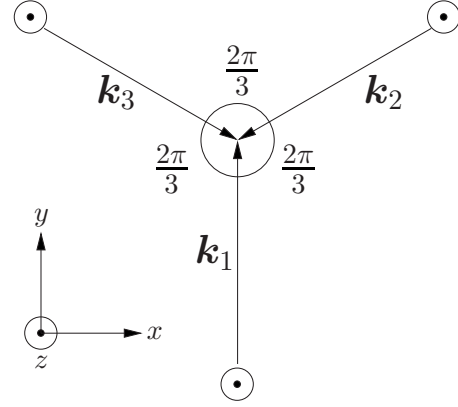tuned light ($\delta<0$) they can be trapped at the field-intensity

FIG. 1. The coplanar three-beam configuration used to generate
the honeycomb lattice. All beams have the same frequency,
strength, and linear polarization orthogonal to their common propagation plane. The honeycomb lattice under consideration is obtained
for blue-detuned beams with respective angles $2\pi/3$. For these
symmetric laser beams, the time-averaged radiation pressure—
albeit small at large detuning—vanishes in this configuration. By
reversing the propagation direction of one of the lasers, such that
$\boldsymbol{k}_1=\boldsymbol{k}_2+\boldsymbol{k}_3$, say, a triangular lattice of a different geometry is
formed. We will, however, exclusively deal with the $\boldsymbol{k}_1+\boldsymbol{k}_2+\boldsymbol{k}_3=0$
case.

maxima. Such arrays of ultracold atoms trapped in optical
lattices have been used in a wide variety of experiments. As
recently evidenced by the observation of the Mott-Hubbard
transition with degenerate gases [24], they have proven to be
a unique tool to mimic, test, and go beyond phenomena observed until now in the condensed-matter realm [14,25].
They also have a promising potential for the implementation
of quantum simulators and for quantum information processing purposes [13,26,27].

B. Optical lattice with honeycomb structure

1. Field configuration and associated dipole potential

The simplest possible optical lattice with honeycomb
structure is generated by superposing three coplanar traveling plane waves that have the same angular frequency ω_L
$=ck_L$, the same field strength $E_0>0$, the same polarization
and the three wave vectors $\boldsymbol{k}_a$ form a trine: their sum vanishes and the angle between any two of them is $2\pi/3$,

$$\boldsymbol{k}_1+\boldsymbol{k}_2+\boldsymbol{k}_3=0, \quad \boldsymbol{k}_a\cdot\boldsymbol{k}_b=k_L^2\left(\frac{3}{2}\delta_{ab}-\frac{1}{2}\right) \qquad (2)$$

with $a,b=1,2,3$ and δ_{ab} is the Kronecker symbol [23]. As is
illustrated in Fig. 1, we choose the x,y plane as the common
plane of propagation and, to be specific, use

$$\boldsymbol{k}_1 = k_L\boldsymbol{e}_y, \quad \left.\begin{array}{c}\boldsymbol{k}_2\\\boldsymbol{k}_3\end{array}\right\} = k_L\frac{\mp\sqrt{3}\boldsymbol{e}_x-\boldsymbol{e}_y}{2} \qquad (3)$$

for the parametrization of the wave vectors.

Further, we take all fields to be linearly polarized orthogonal to the plane, so that the three complex field amplitudes
are given by

$$\mathcal{E}_a(\boldsymbol{r},t) = E_0 e^{i(\boldsymbol{k}_a \cdot \boldsymbol{r} - \phi_a)} e^{-i\omega_L t} \boldsymbol{e}_z, \tag{4}$$

where ϕ_a is the phase of the ath field for $t=0$ at $\boldsymbol{r}=0$. We note that a joint shift of the reference points in time and space,

$$t \to t - \frac{1}{3\omega_L} \sum_a \phi_a, \quad \boldsymbol{r} \to \boldsymbol{r} + \frac{2}{3k_L^2} \sum_a \phi_a \boldsymbol{k}_a, \tag{5}$$

removes the phases ϕ_a from Eq. (4), so that the simple choice $\phi_1 = \phi_2 = \phi_3 = 0$ is permissible, and we adopt this convention. In an experimental implementation, one would need to stabilize the phase differences $\phi_a - \phi_b$ to prevent a rapid jitter of the lattice that could perturb the atoms trapped in the potential minima.

Dipole potential (1) generated by the electric field $\boldsymbol{E} = \Sigma_a \mathcal{E}_a$ is of the form

$$V(\boldsymbol{r}) = V_0 |f(\boldsymbol{r})|^2 = V_0 v(\boldsymbol{r}) \quad \text{with} \quad V_0 = \frac{\hbar\Gamma}{8} \frac{\Gamma}{\delta} \frac{I_0}{I_s}, \tag{6}$$

where I_0 is the intensity associated with the field strength E_0. The total dimensionless field amplitude $f(\boldsymbol{r})$ and the dimensionless optical potential $v(\boldsymbol{r})$ are given by

$$f(\boldsymbol{r}) = 1 + \exp(-i\boldsymbol{b}_1 \cdot \boldsymbol{r}) + \exp(i\boldsymbol{b}_2 \cdot \boldsymbol{r}) \tag{7}$$

and

$$v(\boldsymbol{r}) = 3 + 2\cos(\boldsymbol{b}_1 \cdot \boldsymbol{r}) + 2\cos(\boldsymbol{b}_2 \cdot \boldsymbol{r}) + 2\cos[(\boldsymbol{b}_1 + \boldsymbol{b}_2) \cdot \boldsymbol{r}], \tag{8}$$

where $\boldsymbol{b}_1 = \boldsymbol{k}_3 - \boldsymbol{k}_1$ and $\boldsymbol{b}_2 = \boldsymbol{k}_1 - \boldsymbol{k}_2$ feature the reciprocal primitive vectors. For parametrization (3), we have

$$\left.\begin{array}{c} \boldsymbol{b}_1 \\ \boldsymbol{b}_2 \end{array}\right\} = \kappa \frac{\boldsymbol{e}_x \mp \sqrt{3}\boldsymbol{e}_y}{2} \tag{9}$$

with $\kappa = |\boldsymbol{b}_a| = \sqrt{3}k_L$. One may further notice that the periodic patterns associated to each of the cosine terms in Eq. (8) have the same spatial period of $(2\pi/k_L)/\sqrt{3}$, about 58% of the laser wavelength $\lambda_L = 2\pi/k_L$.

Linear combinations of the Brillouin vectors with integer coefficients define the reciprocal lattice $\widetilde{\mathcal{B}}$, a regular pattern in $\boldsymbol{k}$ space,

$$\widetilde{\mathcal{B}} = \{n_1 \boldsymbol{b}_1 + n_2 \boldsymbol{b}_2 | n_1, n_2 = 0, \pm 1, \pm 2, \ldots\}. \tag{10}$$

The reciprocal lattice is central to all studies of the dynamics of particles that move under the influence of the given periodic potential [28].

In particular, one domain in reciprocal space of utmost importance is the first Brillouin zone Ω defined as the so-called primitive Wigner-Seitz cell [28] of $\widetilde{\mathcal{B}}$; see Fig. 2. It is a *regular* hexagon but with the subtle feature that opposite edges are to be identified with each other since they can be related by a displacement vector in $\widetilde{\mathcal{B}}$. By the same token the three corners K_a (respectively, K_a') have to be identified with one another and we collectively denote them by K (respectively, K'). These two different corners K and K' are known in the graphene literature as the Dirac points for a reason that will become clear in the next section. Upon denoting $\boldsymbol{K}$
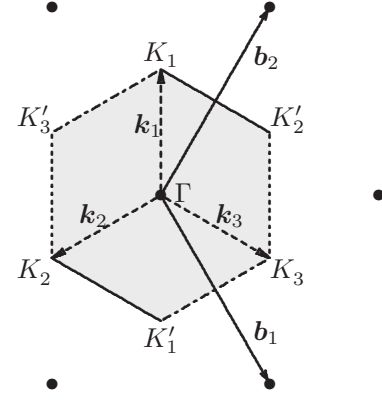

FIG. 2. The triangular reciprocal lattice $\widetilde{\mathcal{B}}$ associated with the triangular Bravais lattice of Fig. 4. It is spanned by the reciprocal primitive vectors $\boldsymbol{b}_1$ and $\boldsymbol{b}_2$ of Eq. (9) and is also a triangular lattice (as indicated by the full dots). The shaded region identifies the first Brillouin zone Ω which is here a regular hexagon. Its center is conventionally named Γ in the solid-state literature. Opposite edges are in fact identical as they only differ by a translation in the reciprocal lattice. This feature is emphasized by drawing the identical edges with the same (solid, dashed, or dash-dotted) line. For the same reason, the three corners K_a ($a=1,2,3$) are to be identified with each other, and likewise the three corners K_a' are really only one point in Ω. Thus, only two of the six corners, collectively labeled as K and K' and known as the Dirac points, are different. Also shown are the wave vectors of the three coplanar plane waves (dashed arrows).

$\equiv \boldsymbol{K}_1$ and $\boldsymbol{K}' \equiv \boldsymbol{K}_1'$, their positions in Ω are given by the wave vector of the lasers that generate the optical honeycomb potential,

$$\boldsymbol{K} = -\boldsymbol{K}' = \frac{1}{3}(\boldsymbol{b}_2 - \boldsymbol{b}_1) = \boldsymbol{k}_1, \tag{11}$$

and $\boldsymbol{K}_2 = \boldsymbol{k}_2 = \boldsymbol{K} - \boldsymbol{b}_2$, $\boldsymbol{K}_3 = \boldsymbol{k}_3 = \boldsymbol{K} + \boldsymbol{b}_1$, as well as $\boldsymbol{K}_a = -\boldsymbol{K}_a'$.

2. Triangular Bravais lattice

The dimensionless potential (8) consists of a periodic two-dimensional array of maxima, minima, and saddle points generated by repeated translations of a primitive unit tile called the *basis*. The underlying lattice geometry itself is encapsulated in the associated Bravais lattice $\mathcal{B}$, that is

$$\mathcal{B} = \{m_1 \boldsymbol{a}_1 + m_2 \boldsymbol{a}_2 | m_1, m_2 = 0, \pm 1, \pm 2, \ldots\}, \tag{12}$$

such that the value of the potential is not affected by any displacement $\boldsymbol{R} \in \mathcal{B}$, $v(\boldsymbol{r}+\boldsymbol{R}) = v(\boldsymbol{r})$.

The Bravais primitive vectors $\boldsymbol{a}_a$ are constructed based on the relation

$$\boldsymbol{a}_a \cdot \boldsymbol{b}_b = 2\pi\delta_{ab}. \tag{13}$$

In other words, the Bravais lattice $\mathcal{B}$ and the Brillouin lattice $\widetilde{\mathcal{B}}$ constitute dual spaces. Supplementing Eq. (9), we have the explicit parametrization
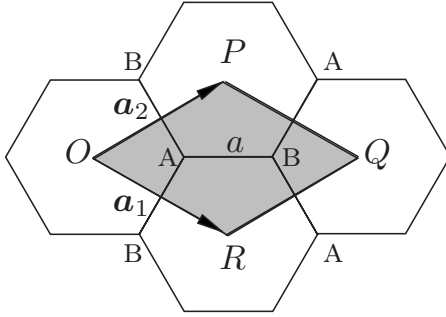
FIG. 3. The underlying Bravais lattice $\mathcal{B}$ of a two-dimensional honeycomb is the two-dimensional triangular Bravais lattice with a two-point basis A and B. The gray-shaded area is the primitive cell Σ. The honeycomb lattice constant a is defined as the distance between nearest-neighbor sites.

$$\left.\begin{array}{c} \boldsymbol{a}_1 \\ \boldsymbol{a}_2 \end{array}\right\} = \Lambda \frac{\sqrt{3}\boldsymbol{e}_x \mp \boldsymbol{e}_y}{2}, \qquad (14)$$

where $\Lambda = |\boldsymbol{a}_a| = 4\pi/(3k_L) = 2\lambda_L/3$ is the common length of the Bravais primitive vectors.

The Bravais lattice defined by Eq. (14) is a *triangular* one. We opt here for the diamond-shaped primitive cell Σ delineated by the two Bravais lattice vectors as a tiling for optical potential (8); see Fig. 3. Another possible choice would have been the hexagonal Wigner-Seitz cell [28]. This cell is useful when discussing the symmetry group of the lattice.

To proceed further one now needs to analyze the structure of optical potential (8) inside the primitive cell. In passing,

we mention here that red-detuned ($\delta < 0$) lasers give $V_0 < 0$ and there is only one potential minimum in each primitive cell Σ. Upon trapping atoms in these potential minima, one gets a triangular lattice that is not of graphene type. This situation is interesting in view of quantum magnetism and frustration phenomena [14] but it is not the situation we want to study here.

3. Honeycomb structure

When the optical lattice is instead blue-detuned ($\delta > 0$), V_0 is positive and atoms are "weak-field seekers." The potential minima coincide with the minima of the electric field strength and the maxima coincide as well. By choice of coordinate system, the maxima locate at the Bravais sites and the dimensionless potential (8) has its maximal value of $v(\boldsymbol{0}) = 9$ at the corners O, P, Q, R of the diamond-shaped primitive cell Σ; see Fig. 4.

Two different potential minima, given by the zeros of the total dimensionless field amplitude $f(\boldsymbol{r})$, are found in Σ at

$$\boldsymbol{r}_A = \frac{1}{3}(\boldsymbol{a}_1 + \boldsymbol{a}_2) = \frac{\Lambda}{\sqrt{3}}\boldsymbol{e}_x \text{ and } \boldsymbol{r}_B = 2\boldsymbol{r}_A, \qquad (15)$$

respectively. From a crystallographic point of view, Σ is a primitive cell with a *two-point* basis. By applying repeated Bravais translations on Σ, one generates two different sublattices of potential minima, one made up of A-type sites and the other made of B-type sites; see Figs. 3 and 4. Altogether the potential minima are organized in a honeycomb structure reminiscent of the positions of the carbon atoms in graphene sheets.

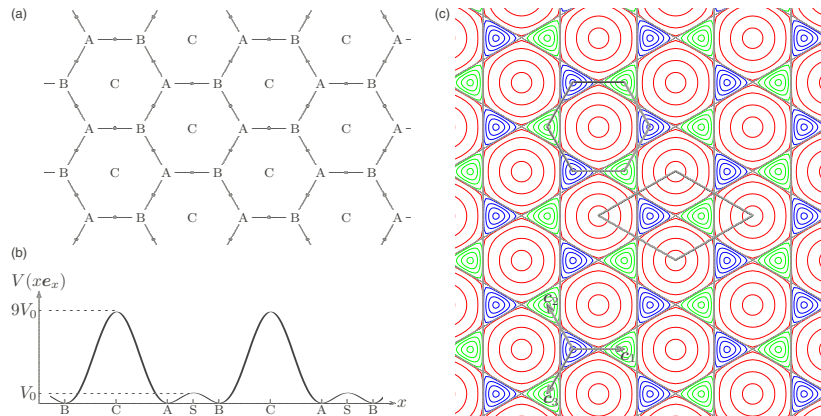The three displacements that move an A site to a neigh-

FIG. 4. (Color online) Left: the honeycomb pattern composed of the triangular lattices of minima at sites A and B, of maxima at sites C, as well as of the saddle points between neighboring A and B sites (marked by dots). The bottom plot shows the potential along the x axis which is one of the ...ABCABC... lines with $x=0$ at a C site. The saddle points S appear as local maxima here, with a height that is one ninth of the global maxima at sites C. Cold atoms trapped in this optical potential would be found at the A and B sites. Right: equipotential lines for the optical honeycomb potential (6). Along the straight black lines that connect the saddle points, we have $V(\boldsymbol{r}) = V_0$. The (red) closed circular curves filling out a hexagonal area are centered at the points of maximal potential; from inside out the respective values are $V(\boldsymbol{r}) = 8V_0, 5V_0, 2V_0$, and $1.05V_0$. The closed curves filling out areas of the shape of equilateral triangles are centered at the minima that constitute the A sublattice (blue) or the B sublattice (green); along the curves the potential has the values $V(\boldsymbol{r}) = 0.95V_0, 0.6V_0, 0.3V_0$, and $0.05V_0$. One primitive diamond-shaped unit tile Σ spanned by $\boldsymbol{a}_1$ and $\boldsymbol{a}_2$ is traced out. It contains two different minima, one of A type (in blue, on the left inside) and one of B type (in green, on the right inside). The trine of the A $\rightarrow$ B displacement vectors (16) is indicated as well. Finally, for completeness, we also trace out the Bravais Wigner-Seitz unit tile. It is a hexagon centered at a potential maximum and with potential minima at its corners.

boring B site—they translate the A sublattice to the B sublattice—are parametrized by

$$c_1 = \frac{1}{3}(a_1 + a_2) = a e_x,$$

$$c_2 = \frac{1}{3}(a_2 - 2a_1) = a \frac{-e_x + \sqrt{3} e_y}{2},$$

$$c_3 = \frac{1}{3}(a_1 - 2a_2) = a \frac{-e_x - \sqrt{3} e_y}{2}, \qquad (16)$$

where $a = |c_j| = \Lambda/\sqrt{3} = 4\pi/(3\kappa) = 2\lambda_L/\sqrt{27}$ is the honeycomb lattice constant. It is the distance from an A site to a neighboring B site or the distance from the center of the hexagon of minima to one of its corners.

Halfway between two neighboring minima, the potential has saddle points where $v(r) = 1$. They are located at the center and at the middle of the edges of Σ; see Fig. 4. As the saddle points on opposite sides of Σ are connected by Bravais displacements, there are, therefore, three nonequivalent triangular sublattices of saddle points and we thus count three saddle points per primitive cell.

We also note that the potential is invariant under 120° rotations around the locations of the potential minima and maxima and, therefore, that the potential is isotropic in the vicinity of these points. We anticipate that the local harmonic oscillator potential at a minimum will be isotropic; see Eq. (35) below. By contrast, the corresponding local potential at a saddle point is not isotropic.

All these matters are illustrated in Fig. 4, where we clearly identify the various triangular sublattices. Cold fermionic atoms trapped in this optical potential would be found at the A and B sites, similar to the binding of electrons in graphene to the carbon ions.

As a side remark, it may be worth mentioning that the saddle points affect the classical dynamics of a particle evolving in the honeycomb potential with a sufficiently large energy. Since the potential is nonseparable and angular momentum is not conserved here, the saddle points could be the seed for instabilities in which case the motion could turn out to be nonintegrable and chaotic. If so, this chaotic behavior should then be revealed, for example, in the statistical properties of the quantum spectra, whose level spacing fluctuations are expected to be described by the Gaussian orthogonal ensemble [29].

4. Optical honeycomb potential and graphene

In graphene sheets, the electrostatic potential that governs the dynamics of electrons, the sum of the Coulomb potentials of the carbon ions, exhibits the symmetries associated to a honeycomb pattern. Of course, in the finer details, the optical dipole potential of Eqs. (6) and (8) differs markedly from the graphene potential. In particular, the very strong forces that the electrons in graphene experience close to the ions have no counterpart in the optical lattice and the interaction between the atoms loaded into the optical potential is quite different from the electric repulsion between electrons. Nev-

ertheless, the common symmetry group implies great similarities between the band structures of the two potentials, and in the respective parameter regimes where the tight-binding approximation is valid, the effective Hamilton operators are virtually identical. In particular, experiments made with atoms offer new knobs to play with and, with due attention to the difference between the two physical systems, these observations may deepen our understanding about phenomena observed with graphene samples.

In a very definite sense, honeycomb potential (6) is the simplest of all graphene-type potentials [30]. Their general form is a Fourier sum over the Brillouin vectors,

$$V(r) = \sum_{Q \in \tilde{\mathcal{B}}} e^{iQ \cdot r} v_Q \quad \text{with} \quad v_{-Q} = v_Q^*. \qquad (17)$$

The various symmetry properties of a honeycomb potential ensure that the v_Qs are grouped into sets of closely related coefficients. If one coefficient in Eq. (17) is nonzero, a whole set of closely related coefficients have corresponding nonzero values as well.

Other than the trivial constant solution $V(r) = v_0$, the simplest case is obtained when all coefficients vanish except for the set associated with $v_{b_1} = V_0$ and, by convention, $v_0 = 3V_0$. This yields honeycomb potential (6) with $v(r)$ of Eq. (8).

III. MASSLESS DIRAC FERMIONS

A. Band structure in the hopping picture

In the hopping picture, one envisions the particle as hopping from site to site with some quantum mechanical hopping (or tunneling) amplitude. In the simplest situation, all sites have the same energy, only hops between nearest-neighbor sites are considered, and all hopping amplitudes take on the same complex value t_0. The one-particle quantum dynamics is then conveniently described using second quantization. In the present situation, as we have two different sublattices, one has to introduce two sets of fermionic annihilation and creation operators, one for the A sites, $(a_{i\sigma}, a_{i\sigma}^\dagger)$, and one for the B sites $(b_{j\sigma}, b_{j\sigma}^\dagger)$, where i and j label the sites in the two-dimensional lattices while σ stands for the spin index or any other pertinent quantum number of the particle. The second-quantized Hamilton operator then reads

$$H = \sum_{\langle i,j \rangle, \sigma} (t_0 b_{i\sigma}^\dagger a_{j\sigma} + t_0^* a_{i\sigma}^\dagger b_{j\sigma}) + \epsilon \sum_{i\sigma} (a_{i\sigma}^\dagger a_{i\sigma} - b_{i\sigma}^\dagger b_{i\sigma}),$$
$$(18)$$

where $\langle i,j \rangle$ means that only nearest neighbors are included in the sum. The model defined by this Hamilton operator accounts for hopping to neighboring lattice sites but does not permit a change in the internal quantum number σ during the hop. We have also included a possible energy mismatch ϵ between the A and B sites [3]. Using the Fourier transform in Ω of the fermionic operators, the right-hand side of Eq. (18) can be recast into the form

$$H = \sum_{k \in \Omega, \sigma} (a_{k\sigma}^\dagger, b_{k\sigma}^\dagger) \begin{pmatrix} \epsilon & z_k \\ z_k^* & -\epsilon \end{pmatrix} \begin{pmatrix} a_{k\sigma} \\ b_{k\sigma} \end{pmatrix} \qquad (19)$$

with

$$z_{\boldsymbol{k}} = t_0 \sum_n e^{i\boldsymbol{k}\cdot\boldsymbol{c}_n}, \tag{20}$$

from which we get the band spectrum

$$\epsilon_{\pm}(\boldsymbol{k}) = \pm\sqrt{\epsilon^2 + |z_{\boldsymbol{k}}|^2}. \tag{21}$$

As expected from the fact that the honeycomb lattice consists of two distinct sublattices, we find two bands: a conduction band (+) and a valence band (−). These bands are here independent of the spin index σ meaning that each $\boldsymbol{k} \in \Omega$ accommodates $2\sigma+1$ internal states per subband. Without any real loss of generality, we will stick to spin-$\frac{1}{2}$ fermions in the sequel. As readily checked, $z_{\boldsymbol{k}}$ vanishes when

$$1 + e^{i\boldsymbol{k}\cdot\boldsymbol{a}_1} + e^{i\boldsymbol{k}\cdot\boldsymbol{a}_2} = 0, \tag{22}$$

which is solved by the corners K and K' of Ω since $\boldsymbol{K}\cdot\boldsymbol{a}_2 = \boldsymbol{K}'\cdot\boldsymbol{a}_1 = 2\pi/3$. We thus see that the conduction and the valence bands are gapped by ϵ, a situation typical of a metal when the lattice is filled with particles. When there is exactly one particle per site (a situation known as half-filling), all levels in the valence band are filled at zero temperature and the Fermi energy E_F (the energy of the highest filled level) precisely cuts the energy surface at the K and K' points. In this case the low-energy excitations of the system can be described by linearizing the band spectrum in the neighborhood of K and K'. Denoting by $\boldsymbol{q} = \boldsymbol{p}/\hbar$ the small displacement from either K or K', the linearization of $z_{\boldsymbol{k}}$ gives

$$|z_{\boldsymbol{k}}| \approx \frac{3a|t_0|}{2}|\boldsymbol{q}| = \hbar v_0|\boldsymbol{q}| = |\boldsymbol{p}|v_0, \tag{23}$$

where the quantity $v_0 = 3a|t_0|/(2\hbar)$ is called the *Fermi velocity* in the solid-state community. We adopt this terminology although it is somewhat unfortunate, because it has nothing to do with the standard Fermi velocity $\sqrt{2E_F/m}$, which depends on the actual mass of the particle.

The dispersion relation now takes on the very suggestive form

$$\epsilon_{\pm}(\boldsymbol{p}) \approx \pm\sqrt{m_*^2 v_0^4 + p^2 v_0^2} \tag{24}$$

that is typical of a relativistic dispersion relation with particle-hole symmetry. The effective mass m_*, defined through $\epsilon = m_* v_0^2$, appears thus as the rest mass of the excitations and relates to the energy imbalance of the two sublattices. The Fermi velocity v_0 is the analog of the velocity of light in relativity.

The effective Hamilton operator that is derived from these considerations and describes the dynamics of the excitations around K and K',

$$H = \int \frac{(d\boldsymbol{r})}{(2\pi)^2} \bar{\psi}(\boldsymbol{r}) \begin{pmatrix} i\boldsymbol{\gamma}\cdot\boldsymbol{\nabla} + m_* & 0 \\ 0 & i\boldsymbol{\gamma}\cdot\boldsymbol{\nabla} - m_* \end{pmatrix} \psi(\boldsymbol{r}), \tag{25}$$

where $\psi(\boldsymbol{r})$ is a four-component Dirac spinor encapsulating the excitations around K and K' while $\bar{\psi} = \psi^\dagger \begin{pmatrix} \gamma^0 & 0 \\ 0 & \gamma^0 \end{pmatrix}$ generates an equation of motion that resembles the Weyl-Dirac equation in two dimensions. This is why the name *Dirac points* is given to K and K' (see Refs. [3,9] for more details). In this two-dimensional context, the Dirac matrices are $\gamma^\mu = (\gamma^0, \boldsymbol{\gamma}) = (\sigma_z, i\sigma_x, i\sigma_y)$ in terms of the standard Pauli matrices.
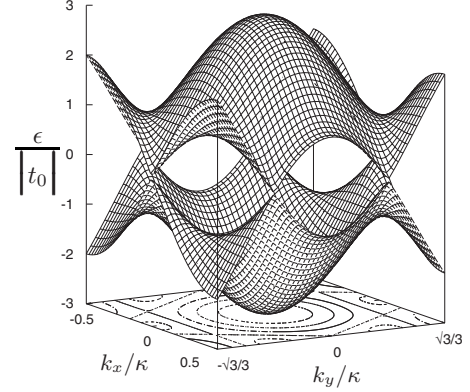

FIG. 5. The tight-binding band structure of graphene (in units of the tunneling strength $|t_0|$) as a function of $\boldsymbol{k} \in \Omega$ in units of $\kappa = \sqrt{3}k_L$. The origin of energy has been chosen at the Dirac points and the axis ranges are $|k_x/\kappa| \leq 1/2$ and $|k_y/\kappa| \leq \sqrt{3}/3$. The bottom contour lines are lines of constant $|\epsilon|/|t_0|$.

When ϵ vanishes, as is the case in real graphene where all lattice sites have the same energy, then $\epsilon_{\pm}(\boldsymbol{k}) = \pm|z_{\boldsymbol{k}}|$ and the two bands are degenerate at the corners of Ω where they display circular conical intersections (see Fig. 5). In the literature, this situation is referred to as a semimetal or a zero-gap semiconductor and the corresponding low-energy excitations are known as massless Dirac fermions. The total band width is $W = 6|t_0|$ and, at half-filling, the Fermi energy $E_F = 3|t_0|$ (taking the energy origin at the lower band minimum) precisely slices the energy bands at the Dirac points. Hence, the Fermi surface reduces to these two points, so that the density of states vanishes there [9]; see Fig. 6.

B. Tight-binding approximation

Mindful of possible experiments, the hopping parameter t_0 appears to be an important amplitude to evaluate. We report three different methods for estimating its strength $|t_0|$. We will start with the familiar tight-binding approximation using localized Wannier functions [31,32] that are further approximated by Gaussians. We will then develop a more
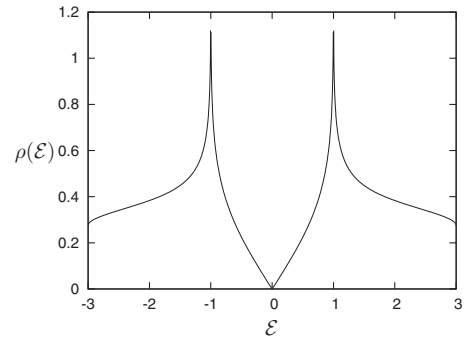

FIG. 6. The noninteracting density of states per unit cell and per spin component $\rho(\mathcal{E})$ as a function of the reduced energy $\mathcal{E} = E/|t_0|$. The origin of energy has been chosen at the Dirac points. When $\mathcal{E} \ll 1$, then $\rho(\mathcal{E}) \approx 2|\mathcal{E}|/(\sqrt{3}\pi)$ and the density of states vanishes at $\mathcal{E} = 0$, a signature of the semimetal behavior. Note the logarithmic Van Hove singularity at $|\mathcal{E}| = 1$.

accurate semiclassical calculation based on an instanton approach [33]. We will compare both results to a brute-force exact numerical computation.

As a consequence of Bloch's theorem [28,34], the energy spectrum of an atom of mass m moving in the honeycomb lattice potential is obtained from

$$\mathcal{H}\psi_{nk}(\boldsymbol{r}) = \left[-\frac{\hbar^2\boldsymbol{\nabla}^2}{2m} + V(\boldsymbol{r}) \right]\psi_{nk}(\boldsymbol{r}) = \epsilon_n(\boldsymbol{k})\psi_{nk}(\boldsymbol{r}), \quad (26)$$

where we dropped the spin index σ which is not essential here. The Bloch waves ψ_{nk} are given by

$$\psi_{nk}(\boldsymbol{r}) = e^{i\boldsymbol{k}\cdot\boldsymbol{r}}u_{nk}(\boldsymbol{r}) \quad (27)$$

with $\boldsymbol{k}\in\Omega$, n the band index, and $u_{nk}(\boldsymbol{r})$ is a $\mathcal{B}$-periodic function. The latter can be conveniently expanded using Wannier functions [28,34,35] in accordance with

$$u_{nk}(\boldsymbol{r}) = \sum_{\boldsymbol{R}\in\mathcal{B}} e^{-i\boldsymbol{k}\cdot(\boldsymbol{r}-\boldsymbol{R})}w_n(\boldsymbol{r}-\boldsymbol{R}). \quad (28)$$

Wannier functions are very useful in describing models where particles are localized in space such as the Hubbard model [36]. They form an orthonormal basis set of functions centered at different Bravais lattice sites which are copies of the same "seed" functions defined in a given primitive cell. The localization properties of the Wannier functions crucially depend on the analyticity properties of u_{nk} as a function of $\boldsymbol{k}$ and decay exponentially in the simple cases [37–40].

In the tight-binding approximation, the atoms are assumed to be sufficiently deeply localized in the different potential wells where they only populate the lowest vibrational levels. Vibrational states in different wells are also assumed to have small overlap: the atomic motion is thus "frozen" except for the small tunneling amplitude between neighboring wells and are then effectively confined to move in the lowest bands of the lattice. Since the Wannier functions display the same symmetry as the local potential structure [41,42], the natural idea here is thus to construct tight-binding Wannier functions from linear combinations of wave functions deeply localized in the two potential wells of the primitive cell (the so-called atomic orbitals) [32,43]. This trial wave function exploits at best the sublattice structure of the honeycomb lattice and should give good results at least for the first two bands.

After dropping the band index n, this approach, reminiscent of the LCAO method (linear combination of atomic orbitals) [28,34], leads to the ansatz

$$\psi_k(\boldsymbol{r}) = \alpha_k\psi_k^{(A)}(\boldsymbol{r}) + \beta_k\psi_k^{(B)}(\boldsymbol{r}), \quad (29)$$

where the quasi-Bloch wave functions

$$\psi_k^{(A)}(\boldsymbol{r}) = \sum_A e^{i\boldsymbol{k}\cdot\boldsymbol{r}_A}w_A(\boldsymbol{r}-\boldsymbol{r}_A),$$

$$\psi_k^{(B)}(\boldsymbol{r}) = \sum_B e^{i\boldsymbol{k}\cdot\boldsymbol{r}_B}w_B(\boldsymbol{r}-\boldsymbol{r}_B) \quad (30)$$

essentially live on the type-A sublattice and the type-B sublattice, respectively. The sublattice Wannier functions $w_A(\boldsymbol{r})$ and $w_B(\boldsymbol{r})$ are normalized to unity. In the present case, we even have $w_B(\boldsymbol{r})=w_A(-\boldsymbol{r})$ due to the reflection symmetry of

the potential, $V(-\boldsymbol{r})=V(\boldsymbol{r})$ [41]. We define the on-site energies as $E_a=\langle w_a|\mathcal{H}|w_a\rangle$ ($a=A,B$) and use the parametrization $E_A=E_0+\Delta$ and $E_B=E_0-\Delta$ in the following, with E_0 the mean on-site energy and Δ half the on-site energy difference. Most importantly, the sublattice Wannier functions are orthogonal. However, obtaining their exact expressions is a difficult task and one often resorts to simple approximations that do not have this property. This is why, in view of this very common practical situation, we will consider in the following that the Wannier functions $w_A(\boldsymbol{r})$ and $w_B(\boldsymbol{r})$ can overlap.

Plugging now the ansatz [Eqs. (29) and (30)] into Eq. (26), and only considering coupling between nearest-neighbor lattice sites, we get the 2×2 homogeneous linear system

$$\begin{pmatrix} \Delta-E & Z_k-ER_k \\ Z_k^*-ER_k^* & -(\Delta+E) \end{pmatrix}\begin{pmatrix} \alpha_k \\ \beta_k \end{pmatrix} = 0, \quad (31)$$

where $E=\epsilon(\boldsymbol{k})-E_0$ and with the matrix entries

$$Z_k = \sum_a t_a e^{i\boldsymbol{k}\cdot\boldsymbol{c}_a},$$

$$t_a = \langle w_A|(\mathcal{H}-E_0)|w_{B_a}\rangle,$$

$$R_k = \sum_a \langle w_A|w_{B_a}\rangle e^{i\boldsymbol{k}\cdot\boldsymbol{c}_a}. \quad (32)$$

Here $B_a=A+\boldsymbol{c}_a$ is a short-hand notation for the three B sites next to the A site.

Several remarks are in order. First one notes that the off-diagonal matrix entries depend on the energy as soon as the sublattice Wannier functions overlap. Second, as readily checked, the hopping amplitudes t_a and E are independent of any energy shift in the Hamilton operator and are thus independent of any particular choice for the energy origin as one expects. Note also that the values of E_A and of E_B do not depend on the particular choice for point A or point B since $\mathcal{H}$ is $\mathcal{B}$-translation invariant. By the same token, the values of t_a and of $\langle w_A|w_{B_a}\rangle$ do not depend on the particular choice of A, but B must be one of its three nearest neighbors.

To have a nonzero solution, the 2×2 determinant associated to Eq. (31) has to vanish, from which we get the band structure. When the overlaps of the sublattice Wannier functions are small, $\langle w_A|w_{B_a}\rangle\ll1$, the band structure is very well approximated by

$$\epsilon_\pm(\boldsymbol{k}) \approx E_0 \pm \sqrt{\Delta^2+|Z_k|^2}, \quad (33)$$

a form reminiscent of Eq. (21). For the honeycomb lattice, for which $\mathcal{H}$ is $\mathcal{B}$ periodic and invariant under reflections, we further have $E_A=E_B=E_0$ and $\Delta=0$, which implies that the effective mass m_* of the Dirac fermions is indeed zero. As a consequence, we get the two first bands as $\epsilon_\pm(\boldsymbol{k})=E_0\pm|Z_k|$. Furthermore, since $V(\boldsymbol{r})$ is also invariant under $2\pi/3$ rotations about any lattice site A, all three tunneling amplitudes t_a from A to B_a acquire the same value and Z_k of Eq. (32) turns into z_k of Eq. (20) with

$$t_0 = \int (d\boldsymbol{r}) w_A^*(\boldsymbol{r})(\mathcal{H} - E_0) w_A(\boldsymbol{r} - \boldsymbol{c}), \qquad (34)$$

where $\mathcal{H}$ is the differential operator of Eq. (26) and $\boldsymbol{c}$ is either one of the three displacement vectors in Eq. (16).

C. Harmonic approximation

To proceed further one needs an approximation for the Wannier functions w_A and w_B. One possibility is to rely on the harmonic approximation of the potential wells around sites A and B, that is, to approximate w_A and w_B by the corresponding harmonic ground-state wave functions. We find

$$V(\boldsymbol{r}_a + \boldsymbol{r}) \approx \frac{3}{4} V_0 \kappa^2 r^2 = \frac{m\omega_0^2}{2} r^2 \quad \text{for} \quad a = A, B$$

$$\text{with} \quad \hbar\omega_0 = 3\sqrt{V_0 E_R}, \qquad (35)$$

where $E_R = \hbar^2 k_L^2 / (2m)$ is the recoil energy of the atom. In terms of $\ell = \sqrt{\hbar/(m\omega_0)}$, the familiar length unit of the harmonic oscillator, the ground-state wave function is

$$w_A(\boldsymbol{r}_A + \boldsymbol{r}) = w_B(\boldsymbol{r}_B + \boldsymbol{r}) \approx \frac{1}{\sqrt{\pi}\ell} \exp\left(-\frac{1}{2} r^2/\ell^2\right). \quad (36)$$

From this we get $E_A = E_B = E_0 \approx \hbar\omega_0$ and the overlap integrals are simply

$$\langle w_A | w_{B_a} \rangle = \exp\left(-\frac{2\pi^2}{9}\sqrt{\frac{V_0}{E_R}}\right). \qquad (37)$$

Keeping in mind that $V_0 \gg E_0 \gg E_R$ in the tight-binding regime, $\langle w_A | w_{B_a} \rangle \ll 1$ and we find from Eq. (34)

$$t_0 \approx -\left(\frac{\pi^2}{3} - 1\right) V_0 \exp\left(-\frac{2\pi^2}{9}\sqrt{\frac{V_0}{E_R}}\right) \qquad (38)$$

at leading order. However, since the hopping amplitude is given by the overlap integral of the localized wave functions w_A and w_B of two neighboring sites, we see that the value of t_0 crucially depends on the tails of these wave functions. Wannier functions often decay exponentially and, therefore, they cannot be realistically approximated by Gaussian wave functions. Hence, Eq. (38) can, at best, serve as a rough underestimate [44]. In the next section we will derive a reliable and accurate estimate of the tunneling amplitudes in the tight-binding regime by use of the instanton method.

D. Semiclassical estimate

Using k_L^{-1}, $\sqrt{V_0/m}$, V_0, and $\sqrt{m/(k_L^2 V_0)}$ as length, velocity, energy, and time units, respectively, the Schrödinger equation can be conveniently recast into a dimensionless form that features an effective Planck's constant $\hbar_e$ (we keep the same symbols for the rescaled variables for simplicity),

$$i\hbar_e \partial_t \psi = -\frac{\hbar_e^2}{2}\boldsymbol{\nabla}^2 \psi + v(\boldsymbol{r})\psi, \quad \hbar_e = \sqrt{\frac{2E_R}{V_0}}, \qquad (39)$$

with $v(\boldsymbol{r})$ given by Eq. (8), here expressed in rescaled units. In the tight-binding approximation it is assumed that V_0

$\gg E_R$, and thus $\hbar_e \ll 1$. In this situation, semiclassical methods provide very efficient and very accurate ways for evaluating dynamical and spectral quantities of interest. They generally amount to evaluating integrals with the aid of semiclassical expressions for the quantum propagator derived from its Feynman-path integral formulation through stationary-phase approximations around the classical trajectories [45].

For example, it is well known that the energy splitting between the two lowest energy levels of an atom moving in a one-dimensional symmetric double well can be accurately calculated using the WKB method [45]. This WKB method can be extended to several dimensions and in the sequel we will derive a semiclassical estimate of t_0 for the honeycomb lattice using the method proposed in [33]. It amounts to evaluating t_0 using the classical complex trajectory (in rescaled units) that connects A and B through the classically forbidden region—the so-called instanton trajectory.

Using $\hbar\omega_0$ as an order of magnitude for the vibrational level inside a potential well, we see that in the rescaled units, this energy is $\hbar\omega_0/V_0 = 3\hbar_e/\sqrt{2} \ll 1$. So we can simply look for the instanton trajectory at zero energy. In rescaled units, the hopping amplitude is then expressed as

$$\frac{|t_0|}{V_0} = \alpha\sqrt{\hbar_e} e^{-S_0/\hbar_e}, \qquad (40)$$

where S_0 is the (rescaled) classical action along the zero-energy instanton trajectory, and the numerical factor α is obtained from integrating out the fluctuations around the zero-energy instanton trajectory (see below).

As the zero-energy instanton fully runs in the classically forbidden region, the variables take on complex values. For our particular case, the good parametrization turns out to keep $\boldsymbol{r}$ real while taking $t = i\tau$ and $\boldsymbol{p} = -i\tilde{\boldsymbol{p}}$ purely imaginary with τ and $\tilde{\boldsymbol{p}}$ real. Hamilton's classical equations of motion in the new variables are just obtained from the original ones by flipping $V(\boldsymbol{r})$ to $-V(\boldsymbol{r})$. The symmetry of the potential dictates that the zero-energy instanton trajectory is simply the straight line connecting site A to B (see Fig. 4). In the following we calculate the instanton between A and A+$\boldsymbol{c}_1$. Integrating the equation of motions, one gets the instanton trajectory in the rescaled form $\boldsymbol{r}_0(\tau) = k_L a x_0(\tau) \boldsymbol{e}_x$ with

$$\tan[\pi x_0(\tau)/3] = -\sqrt{3}\coth[3\sqrt{2}\tau/4]. \qquad (41)$$

The boundary conditions are $x_0 = 1$, $\dot{x}_0 = 0$ when $\tau \rightarrow -\infty$ and $x_0 = 2$, $\dot{x}_0 = 0$ when $\tau \rightarrow \infty$, meaning that the instanton starts at A with zero velocity and ends at B with zero velocity; the whole process requiring an infinite amount of time. This is indeed what is expected as both end points of the instanton are instable in the reversed potential picture. Since the energy associated with this instanton trajectory is zero, the classical action is simply

$$S_0 = \int_{ka}^{2ka} dx |f(x, y = 0)| = 4\sqrt{2}\left(1 - \frac{\pi}{3\sqrt{3}}\right) \approx 2.237, \qquad (42)$$

where $f(\boldsymbol{x}, \boldsymbol{y})$ is given by Eq. (7).

The computation of α proves technically more demanding. Following [33], it is given by the product $\alpha_1\alpha_2$ with

$$\alpha_1 = \sqrt{\frac{S_0}{2\pi}}\sqrt{\frac{\det[-\partial_\tau^2 + \omega_0^2]}{\det'[-\partial_\tau^2 + \omega_x^2(\tau)]}},$$

$$\alpha_2 = \sqrt{\frac{\det[-\partial_\tau^2 + \omega_0^2]}{\det[-\partial_\tau^2 + \omega_y^2(\tau)]}}. \tag{43}$$

Here $\omega_a^2(\tau) = (\partial_a^2 v)(r_0)$ $(a=x,y)$ is the curvature of the rescaled potential along the zero-energy instanton trajectory $r_0(\tau)$ while ω_0 is the curvature of the rescaled harmonic potential approximation around A; see Eq. (35). In rescaled units, we have $\omega_0 = 3/\sqrt{2}$. The prime in the formula for α_1 means that the determinant is calculated by excluding the eigenspace of the operator $-\partial_\tau^2 + \omega_x^2$ with the smallest eigenvalue.

The determinants of the differential operators involved in the computation of α stem from the linear stability analysis of the dynamical flow in the neighborhood of the zero-energy instanton trajectory as encapsulated in the monodromy matrix. They can be straightforwardly computed from solutions of the linear Jacobi-Hill equations of degree 2 associated with these differential operators [46]. For example, α_2 is solved as

$$\alpha_2 = \lim_{T\to\infty}\sqrt{\frac{J_0(T)}{J(T)}}, \tag{44}$$

where the Jacobi fields $J(\tau)$ and $J_0(\tau)$ satisfy the differential equations

$$\frac{d^2J(\tau)}{d\tau^2} - \omega_y^2(\tau)J(\tau) = 0,$$

$$\frac{d^2J_0(\tau)}{d\tau^2} - \omega_0^2 J_0(\tau) = 0, \tag{45}$$

with initial conditions

$$J_0(-T) = J(-T) = 0,$$

$$\dot{J}_0(-T) = \dot{J}(-T) = 1. \tag{46}$$

The interested reader is referred to [33,46] for details. We simply give here the final result for the honeycomb lattice:

$$\alpha_1 = \sqrt{\frac{27\sqrt{2}}{\pi}} \approx 3.486, \quad \alpha_2 \approx 0.449, \quad \alpha \approx 1.565. \tag{47}$$

Recasting the semiclassical calculation of the tunneling amplitude in units of the recoil energy finally yields

$$\frac{|t_0|}{E_R} \approx 1.861\left(\frac{V_0}{E_R}\right)^{3/4}\exp\left[-1.582\sqrt{\frac{V_0}{E_R}}\right]. \tag{48}$$

The same type of scaling laws has been obtained in the case of the two-dimensional square optical lattice [47,44]. In the square-lattice geometry, however, the potential is separable and the semiclassical calculation proves much simpler as it
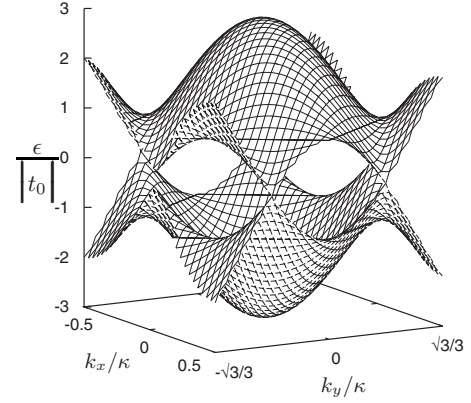

FIG. 7. Numerically calculated band structure of the two lowest energy bands for $\hbar_e = 0.25$ at discrete points in the Brillouin zone Ω. The same conventions as in Fig. 5 are adopted. The value of $|t_0|$ is determined by requiring that $\epsilon_\pm = \pm 3|t_0|$ at the center Γ of the Brillouin zone. The similarity with Fig. 5 shows that at $V_0 = 32E_R$ the tight-binding regime has already been reached.

reduces to using the well-known Mathieu equation.

E. Numerical computation of the band structure

Using Bloch's theorem and plugging Eq. (27) into Eq. (26), we get a family of partial differential equations for the u_{nk}s labeled by the Bloch vector $k \in \Omega$. After scaling variables with the same units as in the previous paragraph, the band structure is then extracted by numerically solving

$$\mathcal{H}_k u_{nk}(r) = \epsilon_{nk} u_{nk}(r),$$

$$\mathcal{H}_k = \frac{\hbar_e^2}{2}(-i\boldsymbol{\nabla} + k)^2 + v(r) \tag{49}$$

for each $k \in \Omega$ (expressed now in units of k_L).

The u_{nk}s being $\mathcal{B}$ periodic, they are conveniently Fourier expanded in the reciprocal lattice $\widetilde{\mathcal{B}}$ according to

$$u_{nk}(r) = \sum_{Q \in \widetilde{\mathcal{B}}} C_{nQ} e^{iQ\cdot r}. \tag{50}$$

The matrix representation of $\mathcal{H}_k$ is sparse and banded. It is then appropriately truncated and diagonalized such that only a small number of coefficients C_{nQ} are actually significant for the corresponding energy bands. The energy bands obtained in this way are exact and one can investigate their dependence on $\hbar_e$ as done in Figs. 7 and 8.

The essential feature is to realize that the band degeneracies at points K and K' are generic and do not depend on the actual value of the effective Planck's constant. Indeed the existence of two degeneracy points in the first Brillouin zone for the honeycomb lattice is a general consequence of the lattice symmetries [48,49]. The lattice symmetries are encapsulated in the point group of the lattice which is the set of operations that leave fixed one particular point of the lattice. The corresponding elements are rotations, reflections, inversions, and their combinations. Combined with $\mathcal{B}$ translations, one gets the space group of the lattice. The graphene point
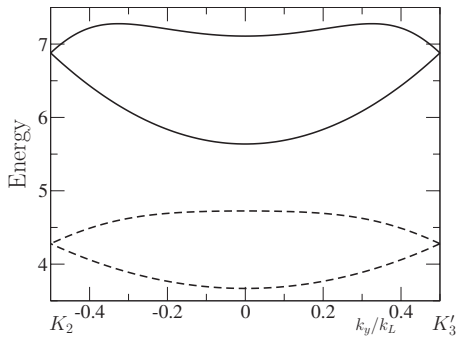
FIG. 8. Band structure for nearly free particles moving in a weak honeycomb optical potential in units of V_0. The first two levels are plotted as a function of k_y/k_L at $k_x/k_L=\sqrt{3}/2$, so along the vertical edge of Ω from K_2 to K_3'; see Fig. 2. The solid curves are obtained for $\hbar_e=\sqrt{2E_R/V_0}=\sqrt{10}$ and the dashed ones for $\hbar_e=\sqrt{5}$. As one can see the band structure is rather flat in the band center but the level curvature increases when $\hbar_e$ is increased. For small V_0 values, the energies of the bands are larger than V_0, that is, above the saddle point separating the A and B sites, emphasizing that the corresponding Bloch states are not anymore localized in these two sites. The Dirac degeneracies in the ground state obtained at the Brillouin zone corners are generic and can be inferred from group-theoretic considerations. Note, however, that the conical intersections do not extend much over the first Brillouin zone when the potential is weak but start to spread when $\hbar_e$ is decreased.

group has been analyzed by Lomer [48] and contains 12 elements. In terms of Bloch wave functions $\psi_{n\mathbf{k}}$, the lattice space-group operations translate into point-group operations on $\mathbf{k} \in \Omega$, possibly followed by a reciprocal lattice translation to bring back the resulting new wave vector in Ω. The key point is that degeneracies can only occur at Bloch wave vectors which are invariant (up to reciprocal lattice translations) under the action of a non-Abelian subgroup G of the point group. For the graphene this happens at the Dirac points. For example, at corner K_1, beside unity, G is made of two rotations of angles $\pm 2\pi/3$ about the center Γ of the Brillouin zone and three reflexions about the lines connecting Γ to the three points labeled K. This group of order 6 admits an irreducible two-dimensional representation which explains the band spectrum degeneracy at the Dirac points.

This can be nicely illustrated in the weak V_0 limit (or equivalently when $\hbar_e$ is large). In this case, the particles are quasifree; i.e., the energies of the bands are larger than V_0, that is, above the saddle point separating the A and B sites (see Fig. 8). The band spectrum can be understood in two steps. First, one folds the parabolic dispersion relation of the free particle into the first Brillouin zone (repeated-zone scheme [28]) and then one couples crossing levels at Bragg planes by the weak potential. At K_1, three plane waves fold with the same kinetic energy, namely, $\mathbf{K}_1=\mathbf{k}_1$, $\mathbf{K}_2=\mathbf{k}_2$, and $\mathbf{K}_3=\mathbf{k}_3$ (see Fig. 2). The weak periodic potential then couples these three plane-wave states and the coupling matrix elements are all identical. The eigenstates of this 3×3 matrix split into a singlet and a doublet. When V_0 is negative, the singlet is the ground state which is consistent with the triangular Bravais lattice obtained in this case ($\delta < 0$). When V_0 is positive ($\delta > 0$), the doublet becomes the ground state and
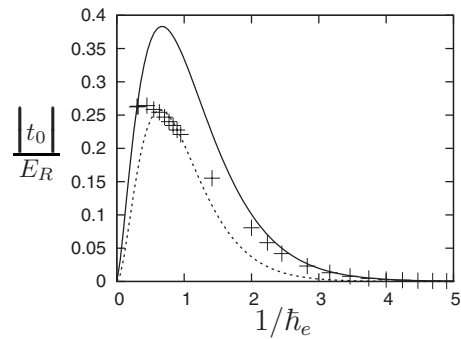

FIG. 9. The hopping parameter $|t_0|$ in units of the recoil energy E_R (crosses) as a function of the inverse of the effective Planck's constant $\hbar_e=\sqrt{2E_R/V_0}$ as obtained from the exact numerical computation. The harmonic approximation (dashed curve) and the semiclassical calculation (solid curve) of the hopping parameter have been added for comparison even if their range of validity is restricted to the tight-binding regime $\hbar_e \ll 1$.

features the tip of the conical intersection between the two subbands when the quasimomentum is moved away from K; see Fig. 8.

From the exact numerical calculation, one can extract the slope of the dispersion relation at the Dirac points and then the corresponding tunneling strength $|t_0|$ as a function of $\hbar_e^{-1}$; see Fig. 9. Figure 10 gives the comparison between the exact calculation, the harmonic, and the semiclassical calculations as a function of $\hbar_e^{-1}$ in the tight-binding regime where $\hbar_e \ll 1$. As one can see, the harmonic approximation is way off whereas the semiclassical estimate proves excellent.

F. Reaching the massless Dirac fermion regime

To access the massless Dirac fermion regime one first needs to completely fill the ground-state band alone, a situation known as half-filling. This is achieved by having exactly one fermion with spin state $\sigma = \pm 1/2$ per Bravais cell.
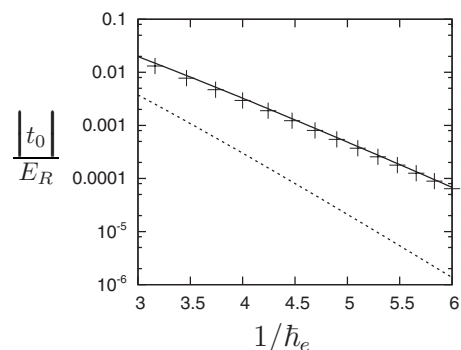

FIG. 10. The hopping parameter $|t_0|$ (in units of the recoil energy E_R) as a function of the inverse effective Planck's constant $\hbar_e=\sqrt{2E_R/V_0}$ in the tight-binding regime where $\hbar_e \ll 1$. As one can see, the harmonic approximation (dashed curve) is completely off. For example at $V_0=32E_R$ (or $\hbar_e=0.25$) $|t_0|$ is underestimated by a factor 10 and the discrepancy gets worse as V_0 increases. On the other hand, the agreement between the semiclassical calculation (solid curve) and the exact numerical computation (crosses) just proves excellent.

Starting from a spin-unpolarized cloud of fermions, half-filling is thus reached by loading the optical honeycomb lattice with exactly two fermions per Bravais cell, corresponding to an average number density $\rho=1$ in the tight-binding picture. When this is achieved, the Fermi energy slices the band structure at the Dirac points. For experiments that study transport phenomena, one would also need to subsequently dope the sample away from half-filling such that the Fermi energy of the system is varied in the linear part of the band structure.

In a usual experiment, atoms are generally held in an external harmonic potential and the optical lattice potential is superimposed. Reaching half-filling could then be done in two steps, first by significantly increasing repulsive interactions U between fermions through a Feshbach resonance and then by driving the system into the Mott-Hubbard phase with one fermion per site as done in [50,51]. Then setting U to zero again should maintain the system at number density $\rho = 1$. Obvious candidates for such experiments are ^{40}K as well as ^{6}Li atoms [50–52]. In the external trap, the Mott insulator appears first where the local filling is approximately one atom per site and one needs to ensure that adding more atoms (or increasing the chemical potential μ) does not favor the appearance of the doubly occupied Mott phase. This will be the case for very strong repulsion $U \gg \mu, t_0, k_B T$ in which case one expects the entire center of the trap to contain a Mott insulating phase with single occupancy and negligible thermally activated doubly occupied sites. In the case of the honeycomb lattice, starting from a spin-unpolarized sample, it is known that half-filling is reached for $U_c \sim 5t_0$, the atoms displaying at the same time an antiferromagnetic order [18]. Note that $U_c \sim W$, where $W=2E_F=6|t_0|$ is the bandwidth.

Doping the system could be done in the following way. The external harmonic confinement (with angular trap frequency Ω_t) defines a characteristic length $\zeta = \sqrt{2|t_0|/(m\Omega_t)}$ over which the energy is shifted by precisely the tunneling energy t_0 [53–55]. This length defines the distance over which one given lattice site is coupled by tunneling to its neighbors. In turn, having loaded N_F fermions into the trap, one can define a characteristic filling factor through $\tilde{\rho} = N_F(a/\zeta)^2$. Varying $|t_0|$ by changing the lattice potential height V_0 or tightening or loosening the trap by changing Ω_t would thus allow to tune $\tilde{\rho}$ in a controlled way and hence to dope the system.

For the conical intersection at the Dirac points to significantly spread over the Brillouin zone Ω, one needs to reach the tight-binding regime where V_0 is large enough (typically $V_0 > 10E_R$ will do). Inspection of the Taylor expansion of Eq. (20) then shows that it is sufficient to have $|q|a \ll 2$ (q being the small displacement from a Dirac point) for the band structure to be well approximated by a linear dispersion relation around the Dirac points. The available energy range ΔE is thus set by the bandwidth itself, namely, $\Delta E \ll W$. So tuning the filling factor away from half-filling and residual thermal fluctuations will keep the system in the massless Dirac fermion regime provided $\mu, k_B T \ll W$ (Fig. 11). For example, at $V_0=32E_R$, the temperature constraint, as derived from Eq. (48), is $T < T_R/50$ whereas it is $T < T_R/2$ at $V_0 =10E_R$. There is thus room left for reaching the massless Dirac fermion regime within the current state-of-the-art cooling technology.
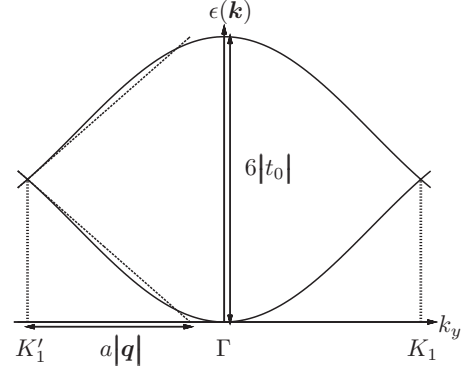

FIG. 11. Cut of the linear dispersion approximation along Oy at $k_x=0$ in the first Brillouin zone Ω as compared to the actual band spectrum in the tight-binding regime. At half-filling, the Fermi energy cuts the band spectrum at the Dirac points K and K'. Doping the system away from half-filling moves the Fermi energy up or down but the system can still be described in terms of massless Dirac fermions provided $a|q| \ll 2$, i.e., provided the change in the Fermi energy is much less than the bandwidth $W=6|t_0|$ itself. By the same token, thermal excitations of the system can still be described as thermal massless Dirac fermions provided $k_B T \ll W$.

IV. ROBUSTNESS OF THE MASSLESS DIRAC FERMIONS

As the very existence of the massless Dirac fermion regime rests on the two conical degeneracies in the band structure, one may wonder if this regime would resist imperfections of the system. Indeed the argument we gave to explain the conical degeneracies relied on group-theoretic arguments which were specific to the hexagonal symmetry of the honeycomb structure. In practice, it is impossible to control the laser configuration to the point where all intensities and alignment angles would all be exactly equal. Such imperfections in the system would obviously break the hexagonal symmetry and one could think that the Dirac fermions would just be destroyed. In fact, as we will see shortly, massless Dirac fermions are quite robust and survive small imperfections that are easily within experimental reach.

A. Imbalanced hopping amplitudes

To understand why massless Dirac fermions are robust, we will start by analyzing the case of imbalanced hopping amplitudes as done in [56]. For real graphene, this would correspond to stretching the graphene sheet. In this case, the tight-binding band structure is given by $\epsilon_\pm(k)=\pm|Z_k|$, where Z_k is defined in Eq. (20). The degeneracies are found at points $k_D \in \Omega$ canceling $Z_k=0$. This condition boils down to sum up three vectors to zero in the two-dimensional plane; see Fig. 12. As such, a solution is only possible provided the hopping amplitudes satisfy one of the norm inequalities given by

$$||t_2| - |t_3|| \le |t_1| \le |t_2| + |t_3| \tag{51}$$

and cyclic permutations. If this is the case, defining the angles $\varphi_{1,2}=\arg t_{2,3}-\arg t_1$, the Dirac points solve

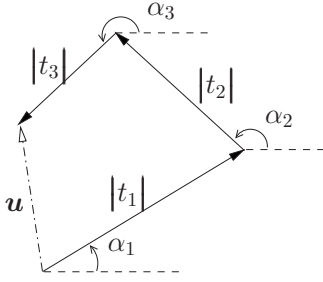$$\cos(\boldsymbol{k}_D \cdot \boldsymbol{a}_1 - \varphi_1) = \frac{|t_3|^2 - |t_2|^2 - |t_1|^2}{2|t_1 t_2|},$$

FIG. 12. The condition $Z_k = 0$ is equivalent to cancel the resultant vector **u** of three vectors, each with length $|t_n|$ and polar angle $\alpha_n = \mathbf{k} \cdot \mathbf{c}_n + \arg(t_n)$. There will always be a solution provided one of the norm inequalities $||t_2| - |t_3|| \leq |t_1| \leq |t_2| + |t_3|$ (and cyclic permutations) is satisfied.

$$\cos(\mathbf{k}_D \cdot \mathbf{a}_2 - \varphi_2) = \frac{|t_2|^2 - |t_3|^2 - |t_1|^2}{2|t_1 t_3|}, \quad (52)$$

subject to the condition

$$|t_2| \sin(\mathbf{k}_D \cdot \mathbf{a}_1 - \varphi_1) + |t_3| \sin(\mathbf{k}_D \cdot \mathbf{a}_2 - \varphi_2) = 0. \quad (53)$$

We find the important result that the system self-adapts to changes in the hopping amplitudes by shifting the Dirac points away from the corners of the Brillouin zone until the norm inequalities (51) break and degeneracies disappear. Thus, provided the hopping imbalance is not too strong, the massless Dirac fermions do survive imperfections in the system and the hexagonal symmetry breaking.

We illustrate this important feature in the simple case of only one imbalanced hopping amplitude, namely, $t_1 = \gamma t_0$ and $t_2 = t_3 = t_0$. We further choose γ real and $0 < |\gamma| \leq 2$ for the Dirac points to exist. We then find two Dirac points D_γ and D'_γ given by $\mathbf{k}_D = -\mathbf{k}'_D = \varphi_0 (\mathbf{b}_2 - \mathbf{b}_1)$ where $\varphi_0 \in [0, 1/2]$ solves $\cos(2\pi\varphi_0) = -\gamma/2$. This means that the two Dirac points D_γ and D'_γ move along opposite paths in the Brillouin zone Ω. The fact that Dirac points always come in by pairs of opposite location in Ω is generic [57]. When γ is increased from 0 to 2, D_γ starts at $\mathbf{k}_0 = (3k_L/4)\mathbf{e}_y$ for $\gamma = 0$, then moves along axis Oy and reach corner K_1 at $\gamma = 1$. Note that when $\gamma \to 0$, the physical situation is that of weakly coupled "zigzag" linear chains. For $\gamma > 1$, D_γ leaves Ω but a translation in reciprocal lattice brings it back on the vertical edges of Ω (technically we get two copies of the same point). D_γ reaches the middle of the vertical edge at $\gamma = 2$ where it merges with D'_γ into a *single* Dirac point; see Fig. 13. Interesting physics occurs at $\gamma = 2$ in connection with the quantum Hall effect [17,58]. As soon as $\gamma > 2$, the degeneracy is lifted and the massless Dirac fermions do not exist anymore. For negative γ, D_γ and D'_γ move back from $\pm(3k_L/4)\mathbf{e}_y$ to the center Γ of the Brillouin zone where they merge and disappear; see Fig. 13. The fact that Dirac points can only merge at the center and mid-edge points of Ω is also generic [57]. Hence, far from being a nuisance, we see that controlling the hopping amplitude imbalance proves an interesting way of exploring the massless Dirac fermions physics under different circumstances by moving around the Dirac points in the Brillouin zone.
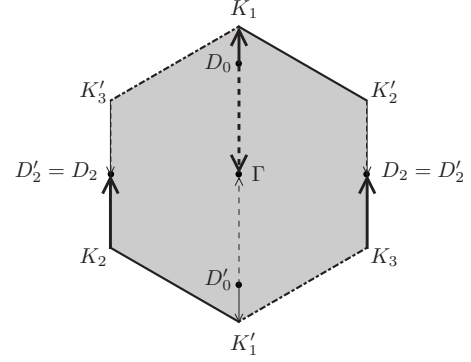

FIG. 13. When the three hopping amplitudes t_n are unbalanced, the Dirac points are shifted in the Brillouin zone Ω and disappear when the norm inequality $||t_2| - |t_3|| \leq |t_1| \leq |t_2| + |t_3|$ is no longer satisfied. We depict here how the Dirac points D_γ and D'_γ move in Ω when only one hopping amplitude is imbalanced, namely, $t_1 = \gamma t_0$ and $t_2 = t_3 = t_0$. Points D_γ (thick path) and D'_γ (thin path) move along opposite paths. Increasing γ from 0, point D_γ starts at D_0 and moves upward. It reaches point K_1 at $\gamma = 1$ (balanced amplitudes case) then moves along the vertical edge of Ω where it reaches its middle point D_2 at $\gamma = 2$. The Dirac points cease to exist when $\gamma > 2$. For negative γ, D_γ moves downward from D_0 (dotted thick path), reaches the zone center Γ for $\gamma = -2$, and then ceases to exist for $\gamma < -2$.

B. Optical lattice distortions

The previous discussion concentrated on the impact of imbalanced hopping amplitudes irrespective of the change in symmetry of the lattice potential. We will now analyze these lattice distortions in more detail and give quantitative estimates about the experimental degree of control which is required to target the massless Dirac fermion regime. We will consider in-plane laser beams with different (positive) strengths $E_n = s_n E_0$ and with respective angles away from $2\pi/3$; see Fig. 14. It is important to note that we will always stick to imperfections which are compatible with a two-point
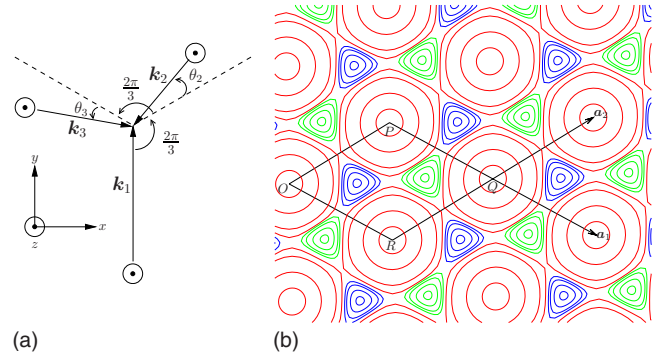

FIG. 14. (Color online) (a) The asymmetric in-plane three-beam configuration. Three monochromatic and linearly polarized laser beams with wave vectors $\mathbf{k}_n$ interfere with different strengths $E_n = s_n E_0$ ($n = 1, 2, 3$). The respective angles depart from $2\pi/3$. (b) Distorted optical lattice obtained with $\vartheta_3 = \vartheta_2 = 5 \times 10^{-2}$ and $s_1 = 1$, $s_2 = 1.03$, and $s_3 = 0.97$. The color convention is the same as in Fig. 4. For weak enough distortions, the primitive diamond-shaped cell Σ still contains two field minima as evidenced in the plot.

Bravais cell. They will only induce distortions of the hexagonal spatial structure of field minima but without breaking this pattern.

The new optical lattice potential is now given by $V'(\mathbf{r}) = V_0|f'(\mathbf{r})|^2$ with the new total dimensionless field amplitude

$$f'(\mathbf{r}) = s_1 + s_2 \exp(-i\mathbf{b}_1' \cdot \mathbf{r}) + s_3 \exp(i\mathbf{b}_2' \cdot \mathbf{r}). \quad (54)$$

Here the $\mathbf{b}_n'$ ($n=1,2$) feature the new reciprocal lattice basis vectors. They define in turn a new set of Bravais lattice basis vectors $\mathbf{a}_n'$ giving rise to a new primitive diamond-shaped cell Σ'. Unless the angle mismatches vanish, the new Bravais and reciprocal lattices are no longer hexagonal but oblique with no special symmetry except for inversion. As a consequence, the new first Brillouin zone Ω' is still a hexagon but *no longer a regular one*.

Since we assume a two-point primitive cell, the minima of the new optical potential still identify with zeros of $f'(\mathbf{r})$. Similarly with the case of imbalanced hopping amplitudes, we find two solutions if and only if the field strengths s_n satisfy one of the norm inequalities $|s_2 - s_3| \leq s_1 \leq s_2 + s_3$ (and cyclic ones). In this case the minima are given by

$$\cos(\mathbf{b}_1' \cdot \mathbf{r}) = \frac{s_3^2 - s_2^2 - s_1^2}{2s_1 s_2},$$

$$\cos(\mathbf{b}_2' \cdot \mathbf{r}) = \frac{s_2^2 - s_3^2 - s_1^2}{2s_1 s_3}, \quad (55)$$

subject to the condition $s_2 \sin(\mathbf{b}_1' \cdot \mathbf{r}) = s_3 \sin(\mathbf{b}_2' \cdot \mathbf{r})$. In the following we will examine separately the effect of strength imbalance and angle mismatch.

1. Critical field strength imbalance

To give an estimate of the critical field strength imbalance beyond which the Dirac points cannot survive, we consider the simple case of only one imbalanced laser beam and no angle mismatch, namely, $\theta_2 = \theta_3 = 0$, $s_1 = 1 + \eta$, and $s_2 = s_3 = 1$. In this case the Bravais lattice, the reciprocal lattice, the primitive cell Σ, and the Brillouin zone Ω are *not* modified. The new optical potential $V'(\mathbf{r}) = V_0 v'(\mathbf{r})$ reads

$$v'(\mathbf{r}) = v(\mathbf{r}) + 2\eta \delta v(\mathbf{r}) + \eta(\eta + 2),$$

$$\delta v(\mathbf{r}) = \cos(\mathbf{b}_1 \cdot \mathbf{r}) + \cos(\mathbf{b}_2 \cdot \mathbf{r}), \quad (56)$$

where $v(\mathbf{r})$ is given by Eq. (8). Note that when only one field strength is imbalanced, the corresponding potential still displays a reflection symmetry. In the present case, it is the Ox-reflection symmetry because $V'(\mathbf{r})$ is invariant under the exchange $\mathbf{b}_1 \leftrightarrow \mathbf{b}_2$. Requiring now that the primitive cell Σ exhibits two field minima imposes $-1 \leq \eta \leq 1$. Their positions in Σ are given by $\mathbf{r}_{A,B}' = \varphi_{A,B}(\mathbf{a}_1 + \mathbf{a}_2)$ with $\cos(2\pi\varphi_{A,B}) = -(1+\eta)/2$. Their midpoint $\mathbf{r}_S' = (\mathbf{r}_A' + \mathbf{r}_B')/2 = (\mathbf{a}_1 + \mathbf{a}_2)/2$ is a saddle point and defines the potential barrier height V_S' to cross to go from A and B in Σ. One finds $V_S' = (\eta - 1)^2 V_0$.

As a whole the field minima organize in a hexagon which is stretched (η negative) or compressed (η positive) along Ox; see Fig. 15. As a consequence two of the three new
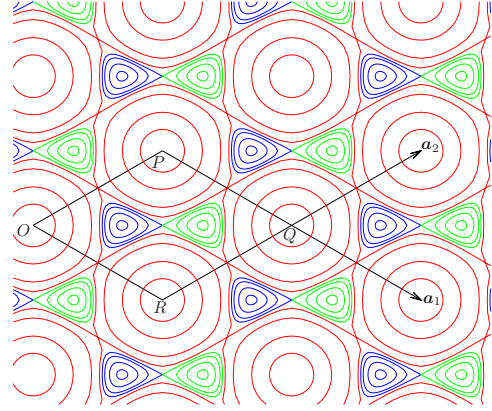

FIG. 15. (Color online) Slightly distorted lattice obtained with vanishing mismatch angles and one imbalanced field strength, namely, $s_1 = 10/9$ and $s_2 = s_3 = 1$. The color convention is the same as in Fig. 4. In this particular case the hexagon of field minima is slightly squeezed along the horizontal axis Ox and the vectors $\mathbf{c}_n'$ connecting a given minimum to its three nearest neighbors have now different lengths. In the situation depicted $|\mathbf{c}_2'| = |\mathbf{c}_3'| \neq |\mathbf{c}_1'|$. In turn, due to the reflection symmetry about Ox, the tight-binding hopping amplitudes satisfy $|t_2| = |t_3| \neq |t_1|$.

vectors $\mathbf{c}_n'$ joining one minimum to its three nearest neighbors will have equal length. In the present situation we get $|\mathbf{c}_2'| = |\mathbf{c}_3'| \neq |\mathbf{c}_1'|$. The potential barrier height V_S'' to cross to go from A to B along $\mathbf{c}_2'$ and $\mathbf{c}_3'$ is given by the corresponding saddle points located at the middle of the edges of Σ. One finds $V_S'' = (\eta + 1)^2 V_0$.

Now, when η is increased from 0, the minima move closer along $\mathbf{c}_1'$ and move away along $\mathbf{c}_2'$ and $\mathbf{c}_3'$. At the same time, the potential barrier V_S' along $\mathbf{c}_1'$ is lowered and the potential barrier V_S'' along $\mathbf{c}_2'$ and $\mathbf{c}_3'$ is increased. As a net effect, in the tight-binding picture, we expect the tunneling amplitude $|t_1|$ to increase while $|t_2|$ and $|t_3|$ decrease. We get the opposite conclusion when η is lowered from 0. Since the potential is invariant through $\mathbf{b}_1 \leftrightarrow \mathbf{b}_2$, we further have $|t_2| = |t_3|$ and we recover the case of one imbalanced hopping amplitude analyzed in the previous section.

One could try to derive a semiclassical expression of the t_n as a function of η using the instanton method but, actually, such a tedious calculation proves unnecessary, at least when η is small. Indeed, by inspection of the semiclassical expression (40), we expect the ratio $|t_1/t_2|$ to scale as $\exp[\Delta S(\eta)/\hbar_e]$ at leading order, where $\Delta S(\eta)$ is the action difference between the two instanton trajectories linking sites A and B along $\mathbf{c}_2'$ and $\mathbf{c}_1'$, respectively. For small enough η we expect $\Delta S(\eta)$ to grow linearly with η, the slope being positive since the ratio $|t_1/t_2|$ should increase with η. The Dirac degeneracies disappear when this ratio is 2 (see previous section), thus we get the semiclassical prediction that this will happen when $\eta \propto \hbar_e$. This result can also be inferred by saying that the Dirac points will disappear as soon as the perturbing potential $2\eta\delta V(\mathbf{r})$, see Eq. (56), strongly mixes the unperturbed states. This will happen when the corresponding coupling energy equals the mean level spacing of the unperturbed system and we get back to the prediction $\eta \propto \hbar_e$.

To check our semiclassical prediction we have computed, for each value of the effective Planck's constant $\hbar_e$, the
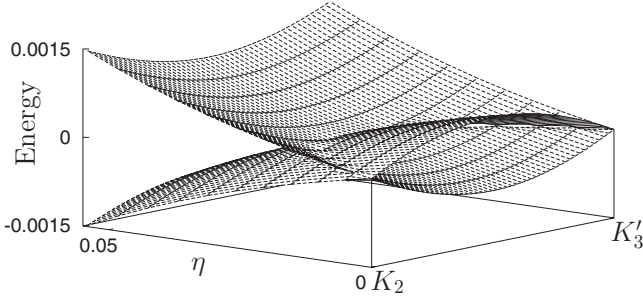
FIG. 16. The band diagram for the two lowest levels as a function of η for $V_0 = 80E_R$ ($\hbar_e \approx 0.158$). The bands are plotted along the vertical straight line joining the Dirac points K_2 and K_3' of the balanced situation; see Fig. 2. The origin of energy is fixed at the Fermi energy for a half-filled band and all bands have been shifted such that the upper and lower bands intersect at zero energy difference.

ground-state and first-excited-state levels for different values of η and we have extracted the corresponding critical value η_c for which the Dirac degeneracies are lifted. Figure 16 gives an example of the band structure obtained at $\hbar_e = 1/\sqrt{40} \approx 0.16$ for η ranging from 0 to 0.054. We have then plotted η_c as a function of $\hbar_e$; see Fig. 17. We have fitted the data with the quadratic fit function $\alpha\hbar_e + \beta\hbar_e^2$ and found $\alpha \approx 0.1074$ and $\beta \approx 0.0624$ enforcing the very good agreement obtained with our linear prediction in the semiclassical regime $\hbar_e \ll 1$. The quadratic correction could certainly be inferred from semiclassical higher-order corrections.

We would like to emphasize at this point that increasing or decreasing η from 0 is not symmetrical. When η is decreased from 0, the Dirac degeneracies are predicted to disappear when $|t_1/t_2| \to 0$. However, the best that we can do is to let $\eta \to -1$. This unfortunately means that one laser beam is almost extinguished and the situation is more that of very weakly coupled one-dimensional chains, a situation we post-
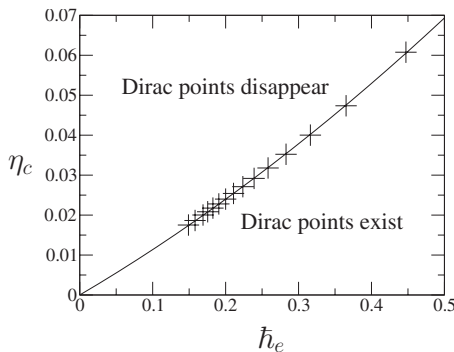

FIG. 17. The critical laser strength imbalance η_c at which the Dirac degeneracies are lifted as a function of the effective Planck's constant $\hbar_e = \sqrt{2E_R/V_0}$. The solid line corresponds to a quadratic fit of the numerical data. The linear coefficient is $\alpha \approx 0.1074$ while the quadratic one is $\beta \approx 0.0624$. As one can see our numerical results are in good agreement with our semiclassical prediction $\eta_c \propto \hbar_e$. The degree of control of the intensity imbalance of the laser fields gets more stringent as the optical lattice depth V_0 is increased. Nevertheless, at already $V_0 = 20E_R$ ($\hbar_e \approx 0.3$), the laser intensities should all equal within 8% which does not sound particularly demanding.
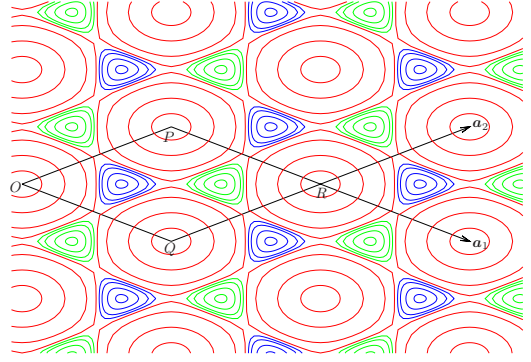

FIG. 18. (Color online) Distorted lattice obtained with balanced field strengths $s_n = 1$ and angle mismatch $\theta_3 = -\theta_2 = -\pi/10$. The color convention is the same as in Fig. 4. In this particular case the hexagon of field minima is stretched along the horizontal axis Ox and the vectors $\boldsymbol{c}_n'$ connecting a given minimum to its three nearest neighbors have now different lengths. In the situation depicted $|\boldsymbol{c}_2'| = |\boldsymbol{c}_3'| \neq |\boldsymbol{c}_1'|$. In turn, due to the reflection symmetry about Ox, the tight-binding hopping amplitudes satisfy $|t_2| = |t_3| \neq |t_1|$.

pone to future study as it proves interesting for high-T_c superconductivity [59]. We thus see that decreasing slightly η from 0 does not harm the Dirac degeneracies. They move inside Ω but do survive. By contrast, increasing slightly η from 0 does destroy the Dirac degeneracies as soon as $\eta \sim \hbar_e$.

As one can see from the plots, the tolerance about the intensity mismatch of the laser beams increases with $\hbar_e$ or equivalently when the optical lattice depth V_0 decreases. On the other hand, as we already saw, the Dirac cones do not extend much over the Brillouin zone if V_0 is too small. So there is a trade-off to make. The situation is, however, really favorable since the intensity mismatch tolerance is already in the 10% range for $V_0 \sim 10E_R$. This means that the massless Dirac fermions prove quite robust and should be easily accessed experimentally.

2. Critical in-plane angle mismatch

We now estimate the critical angle mismatch when all laser beams have the same intensities ($s_1 = s_2 = s_3 = 1$). We see from Eq. (54) that the new optical potential still displays the exchange symmetry $\boldsymbol{b}_1' \leftrightarrow \boldsymbol{b}_2'$ and thus a reflection invariance with respect to their bisectrix. In the following we stick to the simple case where $\theta_3 = -\theta_2 = \theta$ and θ is small. In this case both the Bravais lattice, the reciprocal lattice, the Brillouin zone Ω and the diamond-shaped primitive cell Σ get modified. The new reciprocal basis vectors turn out to be $\boldsymbol{b}_1' = \boldsymbol{b}_1 + \delta\boldsymbol{b}_1$ and $\boldsymbol{b}_2' = \boldsymbol{b}_2 + \delta\boldsymbol{b}_2$ where $\delta\boldsymbol{b}_1 = (\theta/\sqrt{3})\boldsymbol{b}_2$ and $\delta\boldsymbol{b}_2 = (\theta/\sqrt{3})\boldsymbol{b}_1$. Since the exchange symmetry $\boldsymbol{b}_1 \leftrightarrow \boldsymbol{b}_2$ is again preserved, the new potential continues to display the Ox-reflection invariance. Figure 18 gives a plot of the new potential structure for $\theta = -\pi/10$.

This situation boils down again to the case of one imbalanced tunneling amplitude. Indeed, the angle between the $\boldsymbol{b}_1'$ and $\boldsymbol{b}_2'$ decreases when θ is increased from 0. In turn the angle between the corresponding $\boldsymbol{a}_n'$ increases and the hexagon structure made by the A and B minima get compressed
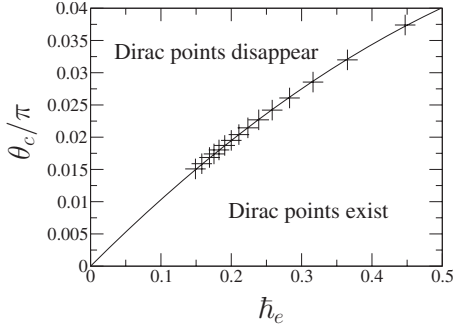
FIG. 19. The critical angle mismatch θ_c (in units of π) beyond which the Dirac degeneracies disappear as a function of the effective Planck's constant $\hbar_e = \sqrt{2E_R/V_0}$. The dashed line corresponds to a quadratic fit of the numerical data. The linear coefficient is 0.109 while the quadratic one is -0.0577. As one can see our numerical results are in good agreement with our semiclassical prediction $\theta_c \propto \hbar_e$. The degree of control of the angle mismatch gets more stringent as the optical lattice depth V_0 is increased. Nevertheless, at already $V_0 = 20E_R$ ($\hbar_e \approx 0.3$), the angle mismatch should be less than $5°$ which is not particularly demanding.

along Ox. The opposite conclusion holds when θ is decreased from 0. We get again the situation where $|t_2| = |t_3| \neq |t_1|$ and $|t_1/t_2| \geq 1$ when $\theta \gtrless 0$ and vice versa. Like for the field strength imbalance, the situations $\theta > 0$ and $\theta < 0$ are not symmetric. The massless Dirac fermions prove more sensitive to *closing* the angle between the $\boldsymbol{b}'_i$, so for $\theta_3 = -\theta_2 = \theta > 0$ because $|t_1/t_2|$ then increases and the threshold $|t_1/t_2| = 2$ is more rapidly hit. This is the situation we explore.

Applying the same reasoning as before, we thus predict the critical angle mismatch beyond which the massless Dirac fermions are destroyed to scale as $\theta_c \propto \hbar_e$. Again, to get θ_c as a function of $\hbar_e$, we numerically compute the band structure at a given $\hbar_e$ for different in-plane mismatch angles θ and then extract the value θ_c for which the Dirac degeneracy is lifted. We then repeat the procedure for different $\hbar_e$. As one can see, our prediction is in very good agreement with the numerical calculations, see Fig. 19, and well supported by a quadratic fit. As θ_c increases with $\hbar_e$, there is a trade-off to make between reaching the tight-binding regime where V_0 is large and achieving an experimentally reasonable angle mismatch tolerance which requires V_0 to be small. The trade-off turns out to be a favorable one since already for $V_0 = 20E_R$ ($\hbar_e \approx 0.3$), one gets a tolerance of about $5°$ on the laser beam alignment. We expect the same type of scaling for small out-of-plane angle mismatches. Furthermore, when several small distortions combine, their effects should add up and thus the critical imperfection threshold should still scale with $\hbar_e$.

As an overall conclusion we see that massless Dirac fermions are quite robust to moderate lattice distortions. Demonstrating them in an experiment should not be particularly demanding in terms of the control of the laser configuration.

C. Inequivalent potential wells

We finally briefly mention how to distort the optical lattice in a systematic manner as it allows for an experimental control of the mass of the Dirac fermions as well as for a continuous switch from a honeycomb lattice to a triangular one. In Sec. II B 4, we observed that honeycomb potential (6) is the simplest of all graphene-type potentials characterized by choosing $v_{\boldsymbol{0}}$ and $v_{\boldsymbol{b}_1}$ real (in fact, positive) while putting all unrelated coefficients in Eq. (17) to zero. Now, letting $v_{\boldsymbol{b}_1}$ to acquire a phase φ, such that $e^{-i\varphi} v_{\boldsymbol{b}_1}$ is positive, will break the reflection symmetry of the honeycomb potential [30].

In the $\boldsymbol{r}$-dependent part of the dimensionless potential (8), this phase φ is introduced by the replacement

$$\sum_{a=1}^{3} \cos(\boldsymbol{b}_a \cdot \boldsymbol{r}) \rightarrow \sum_{a=1}^{3} \cos(\boldsymbol{b}_a \cdot \boldsymbol{r} + \varphi), \quad (57)$$

where $\boldsymbol{b}_3 = -\boldsymbol{b}_1 - \boldsymbol{b}_2$. This can be implemented by superimposing three *independent* standing waves, of the same wavelength and with equal intensity, whose wave vectors form the trine of Fig. 1 [60]. As a consequence of the incoherent superposition, the t replacement of Eq. (5) is not available and the $\boldsymbol{r}$ replacement alone cannot remove all three phases of the standing waves. One can, however, shift $\boldsymbol{r}$ such that the three phases are the same, and then one has an intensity pattern proportional to the right-hand side of Eq. (57).

Most of the hexagon structure of Fig. 4 remains unchanged by this modification: lattice sites A, B, and C continue to be the locations of local minima and maxima, whereas the saddle points S acquire new positions on the ...ABCABC... lines.

Figure 20 confirms that, for small φ values, the minima of the honeycomb dipole potential are still organized in a hexagonal pattern but we now have *different* potential depths at sites A and B. The potential energy mismatch is $2\epsilon \approx 8V_0|\varphi|/\sqrt{3}$. In view of Eqs. (21) and (24), this means that the Dirac fermions acquire a mass $m_* \propto |\varphi|$ or, in other words, that the Dirac degeneracies are lifted. The possibility of fine tuning the mass of the Dirac fermions through the parameter φ is an interesting experimental knob to play with.

Increasing $|\varphi|$ further, one can also see that, for the particular values $|\varphi| = \pi/6$ and $\pi/2$, the three sublattices of saddle points merge into a single triangular lattice, which coincides with the A, B, or C lattice, respectively; see Fig. 20. This merging of a potential minimum or maximum with three saddle points leads to a peculiar third-order saddle point. For $\varphi = \pi/6$, say, the S sites merge with the B sites and we have

$$\sum_{a} \cos(\boldsymbol{b}_a \cdot \boldsymbol{r} + \varphi)\big|_{\varphi=\pi/6} \approx -\frac{1}{6} \sum_{a} [\boldsymbol{b}_a \cdot (\boldsymbol{r} - \boldsymbol{r}_{\mathrm{B}})]^3 \quad (58)$$

for $|\boldsymbol{r} - \boldsymbol{r}_{\mathrm{B}}| \ll \kappa^{-1}$, hence a cubic saddle point rather than the usual quadratic saddle point.

An unpolarized ultracold gas of spin-$\frac{1}{2}$ fermions loaded into such a potential at half-filling would lead to two fermions per well. By driving the system through attractive interactions, one could even get a Mott insulator of fermion pairs. By switching off all interactions and setting $\varphi = 0$, one should be able to study oscillations of atoms between the A and B
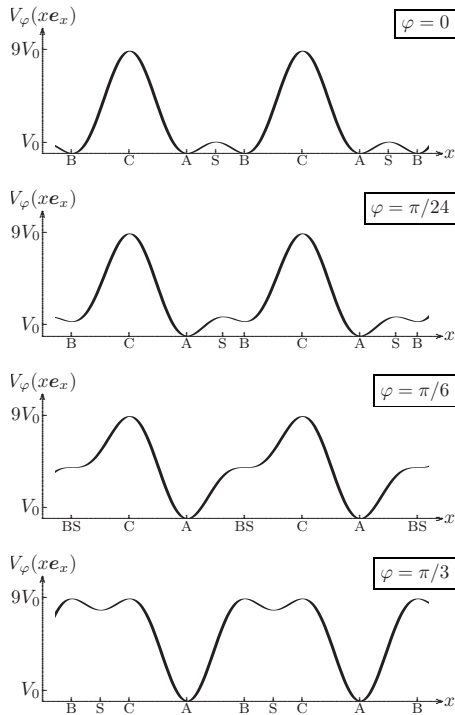
FIG. 20. For various values of the phase parameter φ of Eq. (57), the plot shows the potential energy along a ...ABCABC... line in Fig. 4. The top plot, for $\varphi=0$, repeats the bottom-left plot of Fig. 4 for reference. The degeneracy between sites A and B is lifted for the small φ value of $\varphi=\pi/24$; the saddle points have moved closer to the B sites, where we continue to have local minima. In this situation the Dirac fermions acquire a mass $m_* \propto |\varphi|$. When $\varphi=\pi/6$, the saddle points S coincide with the B sites and we have cubic saddle points there. Finally, in the bottom plot, we have $\varphi=\pi/3$ and the saddle points are halfway between adjacent B and C sites, with potential maxima at both of them. Except for a displacement, the potential in the bottom plot is the negative of the potential in the top plot and thus identical with honeycomb potential (6) for red rather than blue detuning of the three running wave lasers. For ease of comparison, the potential constants are adjusted such that the maxima and minima are at $V=0$ and $V=9V_0$, respectively, for all φ values.

sublattices. We will analyze this situation in a follow-up paper.

V. CONCLUSION

Motivated by the vivid field of graphene physics, we have explained and analyzed how to reproduce massless Dirac fermions by loading ultracold fermions in an optical lattice with honeycomb structure. We have described the two-dimensional laser configuration that gives rise to an optical potential where field minima are organized in a honeycomb structure (with lattice constant a) and we have thoroughly detailed the corresponding crystallographic features. The behavior of atoms propagating in such an optical potential in the tight-binding regime is in one-to-one correspondence with the behavior of electrons propagating in a graphene sheet. The ground-state and first-excited levels of the band structure exhibit two conical degeneracies located at the corners of the first Brillouin zone, as dictated by symmetry arguments. In the neighborhood of these degeneracies, the band spectrum is linear.

When the lattice is loaded with fermions at half-filling, the Fermi energy slices the band structure at these degeneracy points known as the Dirac points. Around half-filling, the tight-binding Hamilton operator can then be recast in a form reminiscent of the relativistic Weyl-Dirac Hamilton operator and featuring so-called massless Dirac fermions. The important parameter driving the dynamics turns out to be the hopping amplitude t_0 between nearest-neighbor sites as it gives the bandwidth $W=6|t_0|$ and the "Fermi velocity" $v_0 = 3a|t_0|/(2\hbar)$. We have derived a semiclassical expression for $|t_0|$ in terms of the effective Planck's constant of the problem, namely, $\hbar_e=\sqrt{2E_R/V_0}$ (with V_0 the optical potential strength and E_R the recoil energy) and have compared it to an exact numerical calculation of the band spectrum. From this we have derived quantitative experimental criteria (such as the required initial temperature of the atomic gas) to reach the massless Dirac fermion regime.

We have also examined the robustness of the massless Dirac fermions to imperfections of the laser configuration (field strengths imbalances and angle mismatches). Massless Dirac fermions turn out to be quite robust as the equality of the beam intensities should be controlled within the few percent range while the respective beam angles should equal $2\pi/3$ within the few degrees range. By appropriately controlling these lattice distortions, one can even control and move the Dirac points in the Brillouin zone. Lastly, we introduce an irremovable phase to the honeycomb potential, hence lifting the degeneracy between two sublattices. In turn, the Dirac fermions acquire a mass proportional to this phase. We also briefly mention the peculiar properties of saddle points and the possibility to study oscillations of atoms between two sublattices as a consequence of this irremovable phase.

As an overall conclusion, mimicking graphene physics with ultracold fermions is within experimental reach. For noninteracting fermions, one could think of implementing transport experiments (in the presence of disorder or not). For example, by rotating the whole honeycomb lattice around a given axis perpendicular to the lattice plane [61] or by implementing the scheme proposed in [62], one would mimic effective magnetic fields able to reproduce the quantum Hall effect situation. In the rest frame of the atoms, the centrifugal effects are described by a fictitious vector potential. This leads to Landau levels and paves the way to physical effects analogous to the quantum Hall effect. The possibility to move the Dirac points in the Brillouin zone even offers new physical effects to test [17].

Interacting systems on a lattice prove also particularly interesting as they can be mapped (at least for strong interactions) on Heisenberg models and thus offer ways of exploring quantum magnetism [63]. In the case of the honeycomb lattice, quantum phase transitions are predicted to occur when the interaction strength $|U|$ is strong enough. For repulsive interactions, quantum Monte Carlo calculations predict antiferromagnetic order to occur at half-filling [18]. For attractive interactions, mean-field calculations have started to

analyze the BEC-BCS crossover and predict a semimetal/superconductor transition [19]. Recent Monte Carlo studies have even started to analyze this BEC-BCS crossover [64] and one can expect an increase in such studies in the near future. On the other hand, Wu and Sarma have begun studies on the higher-energy orbitals on a honeycomb lattice and they conclude that the band structure leads to enhanced interaction effects giving rise to various charge and bond ordered states at commensurate fillings [65]. Very recently, implementations of massless Dirac fermions in square lattices have been proposed [66,67]. The situation seems thus mature for an experimental effort toward loading ultracold fermions in a honeycomb optical lattice.

ACKNOWLEDGMENTS

[1] K. S. Novoselov, A. K. Geim, S. V. Morozov, D. Jiang, Y. Zhang, S. V. Dubonos, I. V. Grigorieva, and A. A. Firsov, Science **306**, 666 (2004).

[2] R. Saito, G. Dresselhaus, and M. S. Dresselhaus, *Physical Properties of Carbon Nanotubes* (Imperial College Press, London, 1998).

[3] G. W. Semenoff, Phys. Rev. Lett. **53**, 2449 (1984).

[4] M. Wilson, Phys. Today **59** (1), 21 (2006).

[5] A. C. Neto, F. Guinea, and N. M. Peres, Phys. World **19** (11), 33 (2006).

[6] S. Y. Zhou, G.-H. Gweon, J. Graf, A. V. Fedorov, C. D. Spataru, R. D. Diehl, Y. Kopelevich, D.-H. Lee, S. G. Louie, and A. Lanzara, Nat. Phys. **2**, 595 (2006).

[7] M. I. Katsnelson, K. S. Novoselov, and A. K. Geim, Nat. Phys. **2**, 620 (2006).

[8] M. I. Katsnelson and K. S. Novoselov, Solid State Commun. **143**, 3 (2007).

[9] A. H. Castro Neto, F. Guinea, N. M. R. Peres, K. S. Novoselov, and A. K. Geim, Rev. Mod. Phys. **81**, 109 (2009).

[10] K. Novoselov, A. Geim, S. Morozov, D. Jiang, M. Katsnelson, I. Grigorieva, S. Dubonos, and A. Firsov, Nature (London) **438**, 197 (2005).

[11] Y. Zhang, Y. Tan, H. Stormer, and P. Kim, Nature (London) **438**, 201 (2005).

[12] G. Li and E. Andrei, Nat. Phys. **3**, 623 (2007).

[13] I. Bloch, Nat. Phys. **1**, 23 (2005).

[14] M. Lewenstein, A. Sanpera, V. Ahufinger, B. Damski, A. Sen(de), and U. Sen, Adv. Phys. **56**, 243 (2007).

[15] E. Timmermans, P. Tommasini, M. Hussein, and A. Kerman, Phys. Rep. **315**, 199 (1999).

[16] S.-L. Zhu, B. Wang, and L.-M. Duan, Phys. Rev. Lett. **98**, 260402 (2007).

[17] P. Dietl, F. Piéchon, and G. Montambaux, Phys. Rev. Lett. **100**, 236405 (2008).

[18] T. Paiva, R. T. Scalettar, W. Zheng, R. R. P. Singh, and J. Oitmaa, Phys. Rev. B **72**, 085123 (2005).

[19] E. Zhao and A. Paramekanti, Phys. Rev. Lett. **97**, 230404 (2006).

[20] C. Cohen-Tannoudji, J. Dupont-Roc, and G. Grynberg, *Atom-Photon Interactions: Basic Processes and Applications* (Wiley-Interscience, New York, 1998).

[21] H. Wallis, Phys. Rep. **255**, 203 (1995).

[22] R. Grimm, M. Weidemüller, and Y. B. Ovchinnikov, Adv. At., Mol., Opt. Phys. **42**, 95 (2000).

[23] G. Grynberg and C. Robilliard, Phys. Rep. **355**, 335 (2001).

[24] M. Greiner, O. Mandel, T. Esslinger, T. W. Hänsch, and I. Bloch, Nature (London) **415**, 39 (2002).

[25] D. Jaksch, C. Bruder, J. I. Cirac, C. W. Gardiner, and P. Zoller, Phys. Rev. Lett. **81**, 3108 (1998).

[26] D. Jaksch, H.-J. Briegel, J. I. Cirac, C. W. Gardiner, and P. Zoller, Phys. Rev. Lett. **82**, 1975 (1999).

[27] X. Chen, B. Zheng, Z.-C. Gu, B. Yoshida, and I. L. Chuang, Phys. Rev. Lett. **102**, 220501 (2009).

[28] N. W. Ashcroft and N. D. Mermin, *Solid State Physics* (Thomson Learning, United Kingdom, 1976).

[29] O. Bohigas, Nucl. Phys. A **751**, 343 (2005).

[30] The symmetry aspects of honeycomb potential will be discussed in more details in a follow-up paper.

[31] G. Wannier, Phys. Rev. **52**, 191 (1937).

[32] P. Wallace, Phys. Rev. **71**, 622 (1947).

[33] G. Mil'nikov and H. Nakamura, J. Chem. Phys. **115**, 6881 (2001).

[34] M. Marder, *Condensed Matter Physics* (Wiley, New York, 2000).

[35] P. B. Blakie and C. W. Clark, J. Phys. B **37**, 1391 (2004).

[36] J. Hubbard, Proc. R. Soc. London, Ser. A **276**, 238 (1963).

[37] W. Kohn, Phys. Rev. **115**, 809 (1959).

[38] J. des Cloizeaux, Phys. Rev. **135**, A685 (1964).

[39] G. Nenciu, Commun. Math. Phys. **91**, 81 (1983).

[40] C. Brouder, G. Panati, M. Calandra, C. Mourougane, and N. Marzari, Phys. Rev. Lett. **98**, 046402 (2007).

[41] J. des Cloizeaux, Phys. Rev. **129**, 554 (1963).

[42] J. des Cloizeaux, Phys. Rev. **135**, A698 (1964).

[43] S. Reich, J. Maultzsch, C. Thomsen, and P. Ordejón, Phys. Rev. B **66**, 035412 (2002).

[44] I. Bloch, J. Dalibard, and W. Zwerger, Rev. Mod. Phys. **80**, 885 (2008).

[45] M. Gutzwiller, *Chaos in Classical and Quantum Mechanics* (Springer, New York, 1990).

[46] L. Schulman, *Techniques and Applications of Path Integration* (Wiley, New York, 1981).

[47] W. Zwerger, J. Opt. B: Quantum Semiclassical Opt. **5**, S9 (2003).

[48] W. M. Lomer, Proc. R. Soc. London, Ser. A **227**, 330 (1955).

[49] J. Slonczewski and P. Weiss, Phys. Rev. **109**, 272 (1958).

[50] R. Jördens, N. Strohmaier, K. Günter, H. Moritz, and T. Esslinger, Nature (London) **455**, 204 (2008).

[51] U. Schneider, L. Hackermüller, S. Will, T. Best, I. Bloch, T. A. Costi, R. W. Hemes, D. Rasch, and A. Rosch, Science **322**, 1520 (2008).

[52] T. Bourdel, L. Khaykovich, J. Cubizolles, J. Zhang, F. Chevy, M. Teichmann, L. Tarruell, S. J. J. M. F. Kokkelmans, and C. Salomon, Phys. Rev. Lett. **93**, 050401 (2004).

[53] M. Rigol, A. Muramatsu, G. G. Batrouni, and R. T. Scalettar, Phys. Rev. Lett. **91**, 130403 (2003).

[54] M. Rigol and A. Muramatsu, Phys. Rev. A **70**, 043627 (2004).

[55] M. Köhl, H. Moritz, T. Stöferle, K. Günter, and T. Esslinger, Phys. Rev. Lett. **94**, 080403 (2005).

[56] Y. Hasegawa, R. Konno, H. Nakano, and M. Kohmoto, Phys. Rev. B **74**, 033413 (2006).

[57] G. Montambaux, F. Piechon, J.-N. Fuchs, and M. O. Goerbig, e-print arXiv:0904.2117.

[58] M. O. Goerbig, J.-N. Fuchs, G. Montambaux, and F. Piéchon, Phys. Rev. B **78**, 045415 (2008).

[59] P. Lee, N. Nagaosa, and X. Wen, Rev. Mod. Phys. **78**, 17 (2006).

[60] We thank David Wilkowski for telling us about this way of introducing the phase parameter φ into the optical potential.

[61] S. Tung, V. Schweikhard, and E. A. Cornell, Phys. Rev. Lett. **97**, 240402 (2006).

[62] A. S. Sørensen, E. Demler, and M. D. Lukin, Phys. Rev. Lett. **94**, 086803 (2005).

[63] E. Demler, W. Hanke, and S. Zhang, Rev. Mod. Phys. **76**, 909 (2004).

[64] S.-Q. Su, K.-M. Tam, and H.-Q. Lin, e-print arXiv:0902.3242.

[65] C. Wu and S. Das Sarma, Phys. Rev. B **77**, 235107 (2008).

[66] J.-M. Hou, W.-X. Yang, and X.-J. Liu, Phys. Rev. A **79**, 043621 (2009).

[67] N. Goldman, A. Kubasiak, A. Bermudez, P. Gaspard, M. Lewenstein, and M. A. Martin-Delgado, Phys. Rev. Lett. **103**, 035301 (2009).